Scalable architecture for trapped-ion quantum computing using RF traps and dynamic optical potentials

David Schwerdt[1,*,†], Lee Peleg[1,*], Yotam Shapira[1,2,*], Nadav Priel[2,*], Yanay Florshaim[2], Avram Gross[2], Ayelet Zalic[2], Gadi Afek[2], Nitzan Akerman[1], Ady Stern[3], Amit Ben Kish[2], and Roee Ozeri[1,2]

[1] *Department of Physics of Complex Systems, Weizmann Institute of Science, Rehovot 7610001, Israel*

[2] *Quantum Art, Ness Ziona 7403682, Israel*

[3] *Department of Condensed Matter Physics, Weizmann Institute of Science, Rehovot 7610001, Israel*

[*] *These authors contributed equally to this work*

[†] *Corresponding author*

Qubits based on ions trapped in linear radio-frequency traps form a successful platform for quantum computing, due to their high-fidelity of operations, all-to-all connectivity and degree of local control. In principle there is no fundamental limit to the number of ion-based qubits that can be confined in a single 1d register. However, in practice there are two main issues associated with long trapped ion-crystals, that stem from the 'softening' of their modes of motion, upon scaling up: high heating rates of the ions' motion, and a dense motional spectrum; both impede the performance of high-fidelity qubit operations. Here we propose a holistic, scalable architecture for quantum computing with large ion-crystals that overcomes these issues. Our method relies on dynamically-operated optical potentials, that instantaneously segment the ion-crystal into cells of a manageable size. We show that these cells behave as nearly independent quantum registers, allowing for parallel entangling gates on all cells. The ability to reconfigure the optical potentials guarantees connectivity across the full ion-crystal, and also enables efficient mid-circuit measurements. We study the implementation of large-scale parallel multi-qubit entangling gates that operate simultaneously on all cells, and present a protocol to compensate for crosstalk errors, enabling full-scale usage of an extensively large register. We illustrate that this architecture is advantageous both for fault-tolerant digital quantum computation and for analog quantum simulations.

I. INTRODUCTION

Trapped ions have ideal properties to be used as qubits for quantum computing (QC); they feature long coherence times, efficient state preparation and detection techniques, and a high degree of connectivity [1–5]. A quantum register of 1000s of qubits, or more, can be formed, for example, by utilizing an equally spaced crystal of ions in a linear RF Paul trap. Indeed recent years have seen many experimental attempts to work with increasingly larger trapped-ion registers [6–9].

However, there are two practical issues associated with large ion-crystals that impede progress in this direction. The first is heating rates; as the number of ions in the crystal, N, increases, heating of the ions' motional modes due to electric field noise drastically increases. Of particular concern is the axial center-of-mass (COM) mode, whose frequency typically decreases as $1/N$. This mode is especially vulnerable, as electric field noise tends to be spatially uniform and to target low-frequency modes [10, 11]. The resulting significant heating rates prohibit the implementation of high fidelity qubit operations, and might destabilize the ion-crystal.

The second issue with large ion-crystals is spectral crowding. As the size of the crystal increases the frequency of adjacent motional modes becomes tightly spaced. For large ion-crystals with a dense mode spectrum, resolving individual modes becomes challenging; this complicates the implementation of entangling gates between two or more ions, which involves exciting their common motion. Granted, spectral control methods [12, 13] allow for simultaneously targeting multiple modes to achieve desired qubit couplings with high fidelity. While such methods are promising for a moderate, up to 100's, number of ions, they do not generally provide a scalable solution for arbitrarily large ion-crystals. First, the optimal control problems that must be solved to implement these methods becomes intractable for large N. Moreover, there is strong evidence that the minimum achievable gate time is set by the smallest frequency spacing among the motional modes [14]. This implies that gate times scale at least as N^2, making large ion-crystals prohibitively slow for quantum computations.

One active direction for scaling ion traps is the quantum charge-coupled device (QCCD) architecture [15, 16]. This setup involves many spatially separated trapping sites, each containing a small number of ions, where communication between sites is done by shuttling individual ions. Inevitably, this comes at the expense of high overhead in hardware and long circuit duration dominated by ion-shuttling and ion-cooling times. An alternative scale-up approach is using photonic-interconnects in order to link small-scale ion-crystals [17–19]. This method as well involves a high overhead, due to the currently low entanglement rate via the interconnect, leading to slow operations.

Here we propose a scalable architecture for QC based on trapped ions qubits, that maintains the advantages of

a long ion-crystal, while circumventing its challenges. In our proposal, an arbitrarily long ion-crystal is segmented into cells by means of dynamically operated optical potentials, e.g. optical tweezers. In this way, the crystal's motional mode structure is modified such that heating rates reflect only the cell size, and not N. Furthermore, programmable high-fidelity multi-qubit entangling gates can be implemented independently within each cell simultaneously. In addition, we show that mid-circuit measurements, a cornerstone of quantum error correction (QEC) techniques, as well as other central quantum computational tools, are straightforward to implement in an optically segmented ion-crystal.

In this work we generalize the method presented in Ref. [14], and employ qubit-local driving fields that implement programmable multi-qubit entangling gates. The method in Ref. [14] provides a clear physical intuition, an efficient procedure for designing gate drive parameters and a thorough scaling analysis, all of which are relevant to this proposal.

The integration of optical tweezers into ion traps is an active area of research [20–25]. Specifically Refs. [22–25] make use of optical tweezers in order to generate target entanglement operations. In Ref. [20] the authors use tweezers for parallel two-qubit entangling gates, the system's scalability is discussed however there is no treatment of large ion-segments or ion-crystal heating rates. In Ref. [21] the authors consider segmenting an ion-crystal using tweezers, however do not analyze generating large-scale entanglement or connectivity between the segments. Mid-circuit measurements are not discussed in any of the above works. Unlike previous studies, here we detail how to achieve a holistic architecture, incorporating parallel and large-scale entangling operations and mid-circuit measurements, that are needed for large scale QC.

The remainder of this paper is organized as follows. In section II we present an overview of the proposed architecture. In section III we sketch two examples of applications of quantum information processing tasks that are amenable to our architecture: quantum simulation and quantum error correction. An in-depth analysis of our proposed architecture follows. Namely, in section IV we derive the spectral properties of optically segmented traps. In section V we analyze the implication of optical segmentation on the ion-crystal's heating rate. In section VI we present our method for designing high-fidelity multi-qubit logical operations that are not hindered by unwanted crosstalk. Lastly, in section VII we present a protocol for performing mid-circuit measurements.

II. PROPOSED ARCHITECTURE

There are well-established techniques for preparation, control and measurement of trapped-ions based qubits for small-scale registers [26, 27]. We therefore focus mostly on unique aspects of our architecture. We propose a QC architecture in which a long trapped ion-crystal, made of N ions, is segmented into S cells, with each cell containing C computational qubits available for quantum computation and simulation, generating a $C\cdot S$ qubit register. The segments are formed by placing B_A barrier ions between adjacent cells, that are illuminated by an optical trapping potential, i.e. optical tweezers, made of tightly focused laser beams [28, 29], that provide an additional local confinement for the barrier ions.

The key point enabling scalability is that due to the optical segmentation the cells behave as nearly independent quantum registers. Indeed, we show below that both challenges of scaling-up trapped ions based QCs, i.e., ion-crystal stability and the performance of logical operations, both scale with the cell size, C, and not the total number cells, S. Thus the dynamically reconfigurable segmentation removes the fundamental limits on the number of cells and on the number of qubits in the ion-crystal, and accordingly on quantum circuit and simulation size.

A general overview of our scalable architecture, is presented schematically in Fig. 1. In favor of a simple presentation we show segmentation of only $S = 4$ cells, and explicitly highlight $C = 8$ computational qubits (green) per cell. In practice 10s of qubits may be placed in each cell, and the number of cells is theoretically unlimited (vertical dots), forming a large ion-crystal. The cells are separated by B_A barrier ions (dark purple), with the schematic showing $B_A = 2$. B_B additional ions (light green) are placed in the center of each cell and are used for segment re-configuration and mid-circuit measurements, with the schematic showing $B_B = 2$. Thus, the ion-crystal contains $N = (C + B_A + B_B)\, S + B_A$ trapped ions.

The figure shows a general mode of operation of the QC, with parallel operations along the vertical axis and sequential operations, ordered from left to right, that form computational steps. Specifically, barrier ions are strongly confined with optical trapping potentials (dark purple), generating the $S = 4$ segments in this example (configuration 'A'). At the nth computational step, local and global driving fields simultaneously implement unitary operations, $U^{(A)}_{s,n}$ (blue), with $s = 1, 2, ..., S$. These unitary operators implement components of the overall quantum algorithm, and may involve all C (green) computational qubits and B_B (light-green) auxiliary ions which are not optically confined in this configuration.

Next all B_A and B_B barrier ions are optically confined, enabling mid-circuit measurement of the auxiliary ions as well as recooling of the ion-crystal and preparation of ions to be used as auxiliary ions (detailed below). Classical feedback (orange arrows), based on the mid-circuit measurement results, may be implemented at this step in order to influence the next layer of unitary evolution.

Next, the segmentation is reconfigured by strongly confining previously unconfined B_B barrier ions and removing the confinement of the B_A barrier ions, thus interchanging their roles. This dynamically and quickly gen-

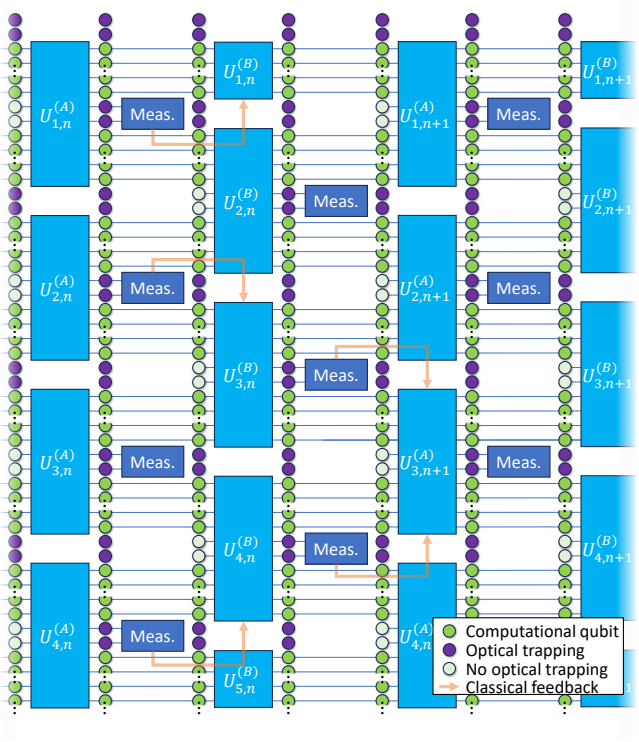

FIG. 1. Architecture for scalable trapped-ion quantum computing using RF traps and dynamic optical potentials. The ion-crystal (vertical direction) is segmented to cells by dynamically applying optical trapping potentials. This generates S segments, each containing C computational qubits (green) that are separated by B_A consecutive optically confined 'barrier ions (dark purple). Additional B_B ions in each cell (light-green) are used to support additional segmentation configurations of the ion-crystal, and mid-circuit measurements ('Meas.') that enable classical feedback (orange arrows) for the implementation of e.g. quantum error correction. For simplicity the schematic shows only 4 segments with 8 computational qubits per cell, however in practice our proposal supports 10s of qubits per cell and an arbitrary number of segments (vertical dots). The horizontal direction shows a typical mode of operation of the QC, namely logical operations, involving multi-qubit logical gates, $U^{(A)}_{s,n}$, are performed in each cell, s, at the nth computational step. The optical potentials are then switched to a different segmentation configuration, allowing for large-scale connectivity between cells of the previous configuration, $U^{(B)}_{s,n}$. Thus ultimately guarantying connectivity between all computational qubits. An intermediate segmentation configuration, in which all B_A and B_B ions are optically confined, is used to accommodate for mid-circuit measurement, cooling of the ion-crystal and state re-initialization.

erates a different configuration of the segments (configuration 'B'). Unitary operators, $U^{(B)}_{s,n}$, can now be implemented and connect previously uncoupled qubits. Additional measurement and re-configuration steps can be applied as required. We remark that here we have shown only two basic ion-crystal configurations (A and B), and have further considered here and below $B_A = B_B$, however various additional segmentation configurations, with different parameters, can be flexibly generated provided relevant ions are allocated as barrier ions.

In addition to the configurable optical trapping potentials, we make use of local independently and simultaneously applied coherent driving fields. As we show below, using these local fields for controlling just one of the atomic transitions of the trapped ions is enough in order to accommodate for programmable multi-qubit logical gates [14], which occur simultaneously in all cells ($U^{(A)}$s and $U^{(B)}$s in Fig. 1), as well as for the mid-circuit measurements and the state preparation that they entail.

III. APPLICATION DEMONSTRATIONS

We sketch examples of applications that showcase the utility of our architecture. These examples rely on various features of our proposal, e.g. implementing large-scale multi-qubit entangling operations and performing mid-circuit measurements. The methods underlying these features are thoroughly discussed and analyzed in the sections below.

We start by considering analog quantum simulations on our system, specifically a three dimensional (3d) quantum-spin model. In general, quantum simulations are considered a well-suited task for noisy intermediate-scale quantum (NISQ) era QCs [30], as simulation of quantum systems is a notoriously challenging task for classical computers, while quantum computers are considered naturally suited for it [31]. Indeed, numerous quantum systems have recently implemented impressive demonstrations of quantum simulations [32–34].

Quantum simulations using trapped-ions based qubits, have also been recently demonstrated [35–42], many of which take advantage of the unique all-to-all coupling present in these systems. In these works Ising-type interactions, that are inherent to trapped ions systems, can be straightforwardly iterated and combined with single-qubit rotations in order to generate arbitrary XYZ-type spin-models [43, 44].

Our architecture is well-suited for quantum simulations, as our ability to design programmable multi-qubit entanglement manifests as the dimensionality and geometry of the simulated model [45], and the optical segmentation and reconfiguration provide a straightforward approach to simulating 3d bulk systems. Such 3d systems are challenging to simulate on linear or planar quantum processors with short-range interactions, due to a large gate overhead required for embedding the 3d geometry.

For simplicity, we focus here on a 3d rectangular lattice of spins, though many other geometries can be realized, e.g. hexagonal. Figure 2 shows an implementation of such a $d \times d \times 2S$ rectangular Ising model. Specifically, Fig. 2(a) shows a single cell of the ion-crystal, that contains $2d^2$ computational qubits (green), and encodes a pair of two-dimensional planes of the simulated

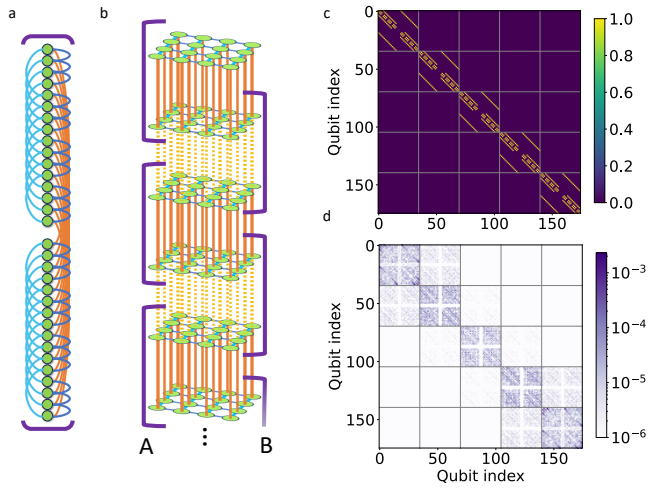

FIG. 2. Quantum simulation of a 3d rectangular Ising spin-model on an optically segmented ion-crystal. Computational qubits (green) are coupled in cells (purple brackets) such that each cell holds two planes of the rectangular spin-model, and implements inter-plane (dark-blue and bright-blue links) and intra-plane (orange links) couplings (a) Couplings of a single cell, holding two planes of the model, with $d = 4$, used for both segmentation configurations. (b) Multiple cells form the 3d Ising model. The two optical configurations ('A', 'B' and purple brackets) enable interlaced coupling of the planes (solid orange and dashed yellow, respectively), such that two entanglement operations implement the model's Hamiltonian. (c) We design the control pulses that implement the nearest-neighbor couplings required for the Ising model, here for $d = 4$ and $S = 5$. The resulting coupling between all qubit pairs (horizontal and vertical axes) is shown (color), exhibiting a block-diagonal structure that implements the links shown in (a), for each cell. (d) Deviation of the qubit-qubit coupling from the ideal structure (log scale), showing a low error, that is not limited by crosstalk between adjacent cells, and enables scaling up. The implementation's infidelity scales as the deviations squared, and is here evaluated to 10^{-4} per cell.

system. Programmable entanglement gates implement the required couplings that generate the model's geometry, i.e. inter-plane couplings (dark-blue and bright-blue) and intra-plane couplings (orange). The model is made three dimensional, as shown in Fig. 2(b), by interlacing the vertical couplings between adjacent layers (solid orange and dashed yellow), using the two segmentation configurations (purple brackets).

As an example, we consider a specific realization of our architecture, in trapped $^{40}Ca^{+}$ ions, and utilize it for a $d = 4$ and $S = 5$ realization of a nearest-neighbor Ising model (see further system details in the SM [46]). We design the control pulses that drive the computational qubits, and generate the required entanglement operations for simultaneous XX-coupling of the qubits, in the entire ion-crystal, similarly to the couplings shown in Fig. 2(a). For simplicity, we use a uniform, unity coupling between all nearest-neighbor qubits. Our design protocol is presented and discussed below.

We calculate the coupling terms that result from the control pulses that we designed, and plot them in Fig. 2(c), with each point on the plot representing a qubit-qubit coupling between qubits of the corresponding indices (horizontal and vertical axes). The block-diagonal structure that is seen reflects the underlying segmented structure of the ion-crystal. The relative difference between the ideal and the resulting qubit-qubit couplings is shown in Fig. 2(d) in log-scale exhibiting a low coupling error that indicates a high-fidelity and accurate simulation. Indeed, the overall performance of our implementation, simultaneously coupling 160 computational qubits, is evaluated with an infidelity that is better (lower) than 10^{-4} per cell.

We note that with this encoding, a time-step of an XX nearest-neighbor 3d rectangular Ising model can be implemented with only two sequential multi-qubit entanglement gates, such as that shown in Fig. 2(c), which, for $d = 4$ and $S = 5$, would otherwise require the application of 384 sequential two-qubit gates between arbitrary pairs in the quantum register (in general $\mathcal{O}\left(d^2S\right)$ two-qubit gates). By considering more elaborate models, e.g. next-nearest neighbor interactions within the two-dimensional planes, non-uniform couplings between the planes, or larger systems, the two-qubit gate count will increase, while with our method two multi-qubit gates still suffice.

The second example showcases a path towards fault-tolerant quantum computation [47–49]. As shown in 3(a), each segment (purple brackets, 'A') is utilized to encode a single logical error-corrected qubit using a distance-five surface code. The code uses 25 computational qubits to store the logical state, and 12 auxiliary (ancilla) qubits to readout the values of both X and Z stabilizer measurements. The entire set of X stabilizer measurements can be implemented in one step, using a single multi-qubit entanglement gate and mid-circuit measurements. Then, the auxiliary qubits are reinitialized, after which the entire set of Z stabilizers is similarly performed. Clearly cell segmentation does not require 12 barrier ions, thus here most of the 12 auxiliary qubits are implemented by computational qubits in the cell.

Naturally, these stabilizer measurements can be performed across all logical qubits in parallel. Note that not all segments must implement the same operation at any given time; some may, for example, implement X stabilizer measurements while others implement Z stabilizer measurements. Figure 3(b) shows a specific example involving five logical qubits, and a multi-qubit entanglement gate, designed to perform simultaneous X and Z stabilizer couplings, in different cells, throughout the entire ion-crystal. The relative difference between the ideal and the resulting qubit-qubit couplings is shown in Fig. 3(c) in log-scale, exhibiting a low error that indicates a high-fidelity and accurate implementation.

Entanglement between two logical qubits, implemented on independent surface codes, can be achieved, for example, using 'lattice surgery' [50, 51]. In this

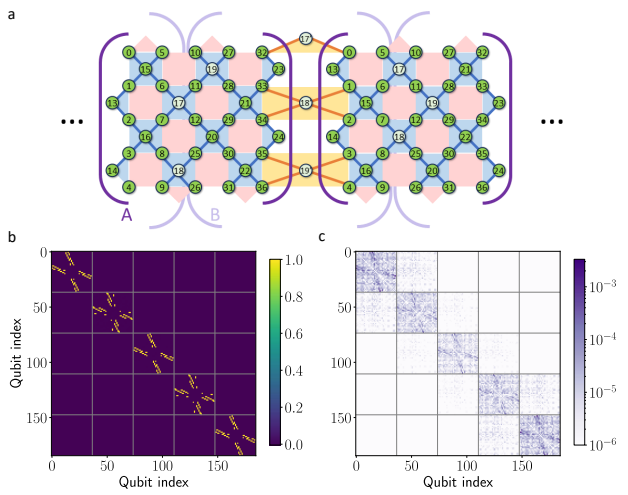

FIG. 3. Quantum error correction code on an optically segmented ion-crystal. (a) We implement several distance-five logical qubits, shown pictorially as grids of 5×5 computational qubits (green). Each cell in configuration 'A' (purple brackets) houses a single logical qubit (labeled 0 - 12 and 25 - 36) and twelve auxiliary qubits (labeled 13 - 24). Programmable multi-qubit gates generate the required entanglement structure for stabilizer measurements on each logical qubit in parallel. Here we show an implementation that generates X-stabilizers (light-blue plaquettes and blue lines). Z-stabilizers may be implemented with an additional gate (light-red plaquettes). Connectivity across the entire register is enabled by configuration 'B' (light-purple brackets) such that each cell in this configuration holds data qubits of two adjacent logical qubits. This enables logical entangling operations between any neighboring encoded qubits via stabilizer measurements formed on the border between the two surface codes (yellow plaqeuttes and orange lines), using the auxiliary ions in this configuration (labeled 17'-19'). (b) Example of programmable multi-qubit gate generating X and Z stabilizers on five logical qubits, implemented on a segmented ion-crystal with $S = 5$, $C = 34$ and $B = 3$. We design the control pulses that implement the entanglement gates required for the various stabilizers. The resulting qubit-qubit couplings between corresponding qubit pairs (horizontal and vertical axes) is shown (color), exhibiting a block-diagonal structure that reflects the formation of five logical qubits. (c) Deviation of the qubit-qubit coupling from the ideal structure (log scale), showing a low error, that is not limited by crosstalk between adjacent cells, and enables scaling up. The gate's infidelity scales as the deviations squared, and is here evaluated to 10^{-4} per cell.

method, stabilizers formed along the border between two surface codes are measured, projecting the joint state of the logical qubits to an entangled basis. In our case, this is naturally enabled by re-configuring the optical segmentation (light-purple brackets, 'B') such that ions from neighboring cells can interact, as shown schematically in Fig. 3 (orange lines and yellow plaquettes). Following this operation, the segmentation reverts to its original configuration, and additional stabilizers are measured. The overall result of this procedure is an entangling logical XX operation between the adjacent surface codes.

We emphasize that even though $S = 5$ is used in this example, our architecture's scalability enables using considerably more cells in order to implement many logical qubits. This example shows one potential route to fault tolerance using our architecture; however many different variants could be considered. First the distance of the code, and thus the number of physical qubits required, should be determined by the demands on the overall logical error rate. Moreover, the choice of the surface code itself, while motivated by its high fault tolerance threshold, is not the only possible choice. In fact, there are other high-threshold codes, with potentially better encoding rates, that may be suitable as well [52]. Constructing an optimal protocol for fault tolerant QC within our architecture, including a prescription for performing logical non-Clifford operations, is a subject for further study.

IV. SPECTRAL PROPERTIES OF OPTICALLY-SEGMENTED ION-CRYSTALS

In general, similar to alternative scale-up methods, segmentation decouples cells from each other, reshaping the well-known all-to-all coupling of trapped ion-crystals to local all-to-all couplings within cells of manageable sizes of tens of ions. As we show below, here this segmentation allows to maintain the ion-crystal's stability as well as to shape programmable multi-qubit quantum gates that act simultaneously and independently within the different cells. Another unique feature of our scale-up strategy, compared to other segmentation approaches, stems from the ability to dynamically and quickly reconfigure the applied segmentation, generating new cells that combine and couple previously decoupled qubits, thus enabling fast and large-scale connectivity within the whole ion-crystal.

We analyze the effect of optical segmentation on the ion-crystal, specifically on collective modes of motion of the ion-crystal in the axial and transverse directions. To this end we assume that the barrier ions are illuminated by beams that generate an optical harmonic trapping frequency of the form [53],

$$\omega_{\mathrm{o.t.p}} = \sqrt{\frac{2\mathrm{Re}[\alpha(\lambda)]}{m}}|E|, \tag{1}$$

where $\alpha(\lambda)$ is the wavelength-dependent polarizibility of an illuminated ion, m is its mass, and E is the field strength. The impact of this potential is best quantified by comparing it to another important parameter in the system, namely the characteristic frequency-scale associated with Coulomb interaction between adjacent ions [20],

$$\nu = \sqrt{\frac{e^2}{4\pi\epsilon_0 m d^3}}, \tag{2}$$

with e the elementary electron charge, ϵ_0 the vacuum permittivity and d is the inter-ion distance of an equidistant ion-crystal. As we show below, a strong optical potential, $\omega_{\mathrm{o.t.p}} > \nu$, drastically changes the motional mode structure of the chain. By incorporating the optical trapping potential with common methods to analyze ion-crystal motion [54], we obtain the normal-mode frequencies and structure in the axial and transverse directions (for further details see the SM [46]).

We first consider the effect of the optical trapping on the axial modes of motion of the ion-crystal, that lie at the lower parts of the motional spectrum and are typically more prone to heating. When considering the joint motional mode structure of two identical ion-crystals, in two completely separate traps, we observe a degenerate mode structure, with each motional frequency appearing twice, and each motional mode being localized at one of the ion-crystals. Thus we intuitively expect that the motional spectrum of a well-decoupled optically segmented ion-crystal will form approximately degenerate bands.

Figure 4 demonstrates this by showing the axial motional spectrum of a $N = 231$ long ion-crystal for a varying optical trapping potential that segments the ion-crystal into $S = 6$ cells, separated by $B_A = 3$ barrier ions, such that each cell contains 35 ions (out of which $C = 32$ are computational qubits and $B_B = 3$ acts as barrier ions for segmentation configuration 'B'). As the optical trapping potential increases the axial spectrum (blue) forms 35 bands of S modes each.

Indeed the formation of bands heralds the decoupling of the motion of cells from each other, such that band frequencies resemble those of an independent, unsegmented, ion-crystal containing $C + B_B$ ions (orange), with each mode in the band being a superposition of local excitations of the corresponding mode of the independent cell. Thus, the width of each band marks the relevant rate in which a motional excitation traverses from one cell to another. That is, an excitation of a local mode in a single cell is composed of a superposition of all modes of the band, which then disperse at a time scale that is inversely proportional to the band width.

Figure 4 further shows B_A high-frequency bands, containing $S + 1$ modes, associated with the motion of $(S + 1)\, B_A$ barrier ions. Crucially these bands are spectrally separated from the 'bulk' ions such that their motion is essentially decoupled from the bulk. We exploit this fact below in order to implement mid-circuit measurements and cooling of the barrier ions.

Figure 5 shows the transverse (radial) band structure of the same $N = 231$ ions systems with $\omega_{\mathrm{o.t.p}}$ set to match the scale of the RF trapping in the transverse direction, ω_{rad}, yielding $\omega_{\mathrm{o.t.p}} \approx 4.2\nu$ (dashed vertical line in Fig. 4). Similarly to the axial direction, optical segmentation results in the formation of $C + B_B$ bulk-bands as well as additional B_A bands associated with the motion of barrier ions (blue). The average frequencies of the bands resemble those of an independent cell (orange), also shown in the inset (bottom right) that presents a zoom-in on the last four computational qubit bands, showing narrow and well-separated bands. For transverse modes of motion the band index, b (horizontal axis), ordered according to the band's frequency, is opposite to the mode's wave vector, i.e. large b's represent long-wavelength modes of motion.

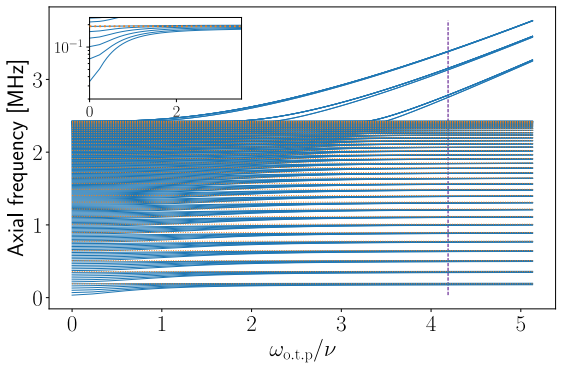

FIG. 4. Axial spectrum of an ion-crystal with N=231 ions, segmented into $S = 6$ cells. Cells are separated by $B_A = 3$ barrier ions and include $C + B_B = 35$ ions each. The axial frequencies (blue) are shown for various trapping optical potentials, $\omega_{\mathrm{o.t.p}}$ and are normalized by the characteristic Coulomb scale, ν. For comparison, an additional axial spectrum of an independent ion-crystal with 35 ions is shown (dashed orange). For $\omega_{\mathrm{o.t.p}} > \nu$ the axial spectrum of the optically segmented trap forms bands which are located at the frequencies of the independent cell. As $\omega_{\mathrm{o.t.p}}$ increases high-frequency bands form, which are due to the B_A barrier ions. The radial trapping frequency, $\omega_{\mathrm{rad}}/\nu \approx 4.2$ (vertical line), is relevant for generating multi-qubit operations. The inset is a zoom-in on the center-of-mass band (vertical axis in log-scale), showing that at $\omega_{\mathrm{o.t.p}} = 2\nu$ the segmented crystal's modes resemble the independent cell, implying that heating is dictated by the properties of a single cell rather than the whole, multi-cell, crystal.

Transverse modes of motion are used in order to generate entanglement between computational qubits, by mediating qubit-qubit interaction via spin-dependent motion. Typically the entanglement operation duration is inversely related to the frequency difference between adjacent modes of motion [14].

Here, the frequency gap between bands, $\Delta\omega_b = \omega_b - \omega_{b-1}$, with ω_b the mean frequency of the modes of bulk bands, $b = 1, ..., C + B_B$, marks the typical interaction rate between ions within the same cell. Thus a simple estimation of unwanted crosstalk in the entanglement operations between cells is given by $\varepsilon_{\mathrm{BW},b} = \frac{\mathrm{BW}_b}{2\Delta\omega_b}$, with BW_b the bandwidth of band b, that sets the coupling rate between cells. The resulting estimate is presented in the inset (top left) of Fig. 5 (orange), showing that high b bands, associated with long-wavelength motion across cells, results in a higher crosstalk, at the few percent level. A more precise estimate of the crosstalk is also shown (blue) and discussed below.

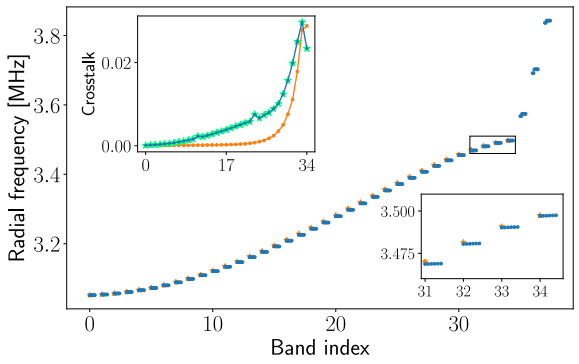

FIG. 5. Radial modes spectrum of an optically-segmented ion-crystal containing $N = 231$ ions, and the resulting cell crosstalk. Due to the segmentation the mode frequencies (blue) form $C + B_B$ bands, which imitate the structure of an unsegmented independent cell (orange). Additional B_A high-frequency bands associated with the barrier ions are formed as well. The bottom-right inset shows a zoom-in on the last four bulk bands. The bands are well separated and narrow in frequency. The top-left inset presents estimations of unwanted crosstalk between cells during simultaneous multi-qubit operations, mediated by the various bulk bands. The estimations are formed by considering only spectral consideration, $\varepsilon_{\mathrm{BW},b}$ (orange) or mode-structure considerations, $\varepsilon_{J,b}$ (blue). Both predict a $\sim$ 2.5% crosstalk due to mainly long-wavelength motion of the cells, associated with high bands. Mitigation of the crosstalk is presented in the main text.

Optically confined ions are not used as computational qubits since optical confinement significantly degrades their coherence due to spontaneous photon scattering and uncontrolled light-shifts. For example, we consider $^{40}Ca^{+}$ ions that are illuminated by a confining optical field at 400 nm with a beam that has a diameter of 1 μm, driving the $S \leftrightarrow P$ transition. In this setup, a harmonic confinement frequency of $\omega_{\mathrm{o.t.p}} = \omega_{\mathrm{rad}} = 3$ MHz, used throughout our analysis, requires an optical power of 50 mw per barrier ion. The resulting photon scattering rate from the P manifold is approximately 10 kHz and the frequency shift of the $S \leftrightarrow P$ transition is approximately 2 GHz. Photons scattered from barrier ions are significantly detuned, by few THz, from this transition in the computational qubits, resulting in a low, < 1 Hz, decoherence rate.

V. HEATING RATES OF OPTICALLY-SEGMENTED ION-CRYSTALS

A crucial criteria for successfully scaling-up ion-crystals is maintaining crystal stability. In the standard approach to trapped ion-crystals this challenge comes about as a heating rate of the crystal that scales unfavorably with N. Specifically, in un-segmented ion-crystals as N increases, the frequencies of low-lying long-wavelength modes of motion decrease, and become more susceptible to electrical noise, leading to degradation of coherent operations, destabilization of the ion-crystal and its eventual melting. Utilizing optical trapping potentials generates cell-local heating rates, which only depend on the cell size, C, and not on the total number of ions N (or S), potentially allowing for arbitrarily long ion-crystals.

This is shown graphically in Fig. 4, since for $\omega_{\mathrm{o.t.p}} \geq 2\nu$ the low-lying COM band is lifted and its frequency converges to the COM mode of an independent cell (inset), implying cell-dependent (and not N-dependent) heating rates. The COM modes remain gapped regardless of N.

We directly quantify the phonon excitation rate of the optically-segmented architecture. For a given motional mode, the phonon excitation Fermi's golden rule rate due to the presence of some electric field noise, $\delta E(t, r)$, is given by [11],

$$\Gamma^{(k)} = \frac{e^2}{4m\hbar\omega_k} S_E^{(k)}(\omega_k), \tag{3}$$

with ω_k the frequency of mode k, and $S_E^{(k)}(\omega_k)$ is the spectral density of the electric field noise. The mode's heating rate is $\hbar\omega_k\Gamma^{(k)}$.

The precise form of the spectral density function is a subject of much theoretical and experimental study [10, 11, 55–59], is system-dependent and its theoretical limits remains somewhat inconclusive. Yet it is generally agreed that it scales as, $S_E(\omega) \propto \omega^{-\alpha} D^{-\beta} T^{\gamma}$, with mode frequency ω, ion-electrode distance D, and temperature, T, and α, β and γ are scaling exponents. Motivated by many experimental results, here we assume that the noisy electric field is spatially uniform along the ion-crystal and that $\alpha = 1$.

Using these consideration we obtain the system's excitation rate (see details in the SM [46]),

$$\Gamma = \sum_k \Gamma^{(k)} \propto \sum_k \frac{e^2}{4m\hbar\omega_k^{1+\alpha}} \sum_{i,j} A_k^{(i)} A_k^{(j)}, \tag{4}$$

with $\Gamma^{(k)}$ the excitation rate of the kth mode and A an orthogonal axial mode-matrix, such that $A_k^{(i)}$ is the participation of the ith ion in the kth axial mode of motion, obtained by analyzing the axial mode structure [46, 54].

Due to the summation over k, our formulation of Γ in Eq. (4) is extensive, e.g. for two identical and independent copies of an ion-crystal, Γ will be evaluated as twice the value of a single copy of the ion-crystal. Thus ideal decoupling between cells in the optically segmented ion-crystal is expected to show-up as proportionality of Γ to S.

Figure 6 shows the predicted excitation rate of the optically segmented ion-crystal, due to Eq. (4), for various values of the cell size, C (horizontal axis), and number of segments, S (colors). The barrier size is set to $B_A = 3$ and each cell contains $C + B_B$ ions, with $B_B = 3$.

Excitation rates are calculated for ion-crystals reaching $N > 1300$ ions. The figure shows, $\Gamma/(\Gamma_{\rm ind}S)$ (vertical axis), such that the excitation rates are normalized by the number of segments, S, and by the excitation rate of an independent unsegmented ion-crystal containing $C+B_B$ ions, $\Gamma_{\rm ind}$. We observe that the normalized excitation rates are all of order unity and converge towards 1 as C increases, with a negligible dependence on the number of segments. Thus we conclude that the cell's stabilization is dominated by cell properties, and is specifically independent from other cells in the ion-crystal.

The main contribution to Γ is given by the lowest frequency band, which is a COM motional band. This is intuitive as COM modes have the lowest motional frequencies, as well as a high overlap with the uniform electric field noise considered here, as compared to other modes which have negligible contributions. This is seen in the dashed lines of Fig. 6 in which we calculate Γ using exclusively this single band (while $\Gamma_{\rm ind}$ is still calculated in full).

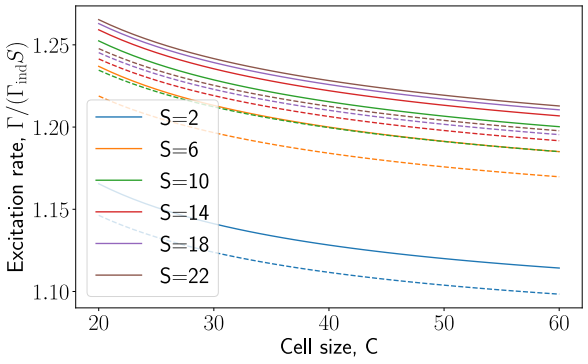

FIG. 6. Axial excitation rate of optically segmented ion-crystals. The excitation rates (vertical axis), Γ, are shown for various values of cell sizes, C (horizontal axis) and number of segments, S (colors). We normalize Γ by the excitation rate of an independent single cell, $\Gamma_{\rm ind}$ and by the number of segments, S. All resulting normalized rates are of order unity, showing that the stability of the optically segmented ion-crystal is dictated by C, and is largely independent of S. We repeat this process but with only considering the lowest band of motional modes in the expression for Γ (dashed), without varying $\Gamma_{\rm ind}$. The resemblance between this result and the full expression of Γ (solid) shows that the lowest-lying band is the dominant contributor to the heating. This result is intuitive as this band is a COM motional band, having a high-overlap with a uniform electric field.

VI. PARALLEL MULTI-QUBIT LOGIC AND CROSSTALK MITIGATION

In trapped ions based quantum computers, logical gates between qubits, i.e. entanglement, is typically facilitated by spin-dependent forces acting on normal-modes of motion of the ion-crystal [60, 61]. Thus adequate control of the normal-mode structure is crucial for scaling-up the trapped ion quantum register size. Specifically, utilizing many modes of motion simultaneously enables programmable long-range interactions [12–14], which are significant for efficient implementation of various quantum computational tasks [52, 62–65]. However utilizing multiple modes of motion becomes increasingly challenging in large ion-crystals due to the overwhelming complexity of the required qubit drive, which comes about as a NP-hard optimization problem [12], as well as an apparent slow-down of the feasible gate duration [14] which, in absence of segmentation, scales as N^2. Thus segmentation plays here a crucial role as well in generating independent large, yet manageable, computational qubit cells.

The heuristic estimation for crosstalk error, provided by $\varepsilon_{\rm BW,b}$ above, can be improved by a detailed consideration of the transverse mode-structure. Specifically, based on the quadratic-form of qubit-qubit entanglement discussed thoroughly in [14], the coupling term between ions c (c') in cells s (s'), mediated by band b, is estimated as

$$J_b^{(c,s),(c',s')} = \sum_{m=1}^{S} R_{(b,m)}^{(c,s)} R_{(b,m)}^{(c',s')}, \tag{5}$$

with R an orthogonal radial mode-matrix (similar to A above) such that $R_{(b,m)}^{(c,s)}$ is the participation of ion c of cell s in mode m of band b (specific examples of $J_b^{(c,s),(c',s')}$ are shown in the SM [46]). Using J_b above, we form a more detailed crosstalk estimation, namely,

$$\varepsilon_{J,b} = \frac{\max\limits_{c\neq c',s\neq s'} \left|J_b^{(c,s),(c',s')}\right|}{\max\limits_{c\neq c',s} \left|J_b^{(c,s),(c',s)}\right|}, \tag{6}$$

with s, s' maximized over all S cells in the segmented ion-crystal and c, c' maximized over all C computational qubits in each of the cells. In essence the estimation in Eq. (6) compares the coupling between ions in the same cell ($s = s'$) to coupling between ions in difference cells ($s \neq s'$). This estimation is also shown in the inset (top-left) of Fig. 5 (blue), exhibiting a similar behavior to that of $\varepsilon_{{\rm BW},b}$, i.e. $\sim 2.5\%$ crosstalk mainly due to long-wavelength motional excitations of the cells. We also evaluate separately the contribution of nearest-neighbor cells, $\varepsilon_{J,b}^{\rm nn}$, which follows the same definition as $\varepsilon_{J,b}$ in Eq. (6) but with $s' = s \pm 1$ in the numerator. This estimation is shown as well in the inset (top-left) of Fig. 5 (green stars), showing an almost exact agreement with $\varepsilon_{J,b}$. Thus we conclude that the $\sim 2.5\%$ crosstalk is mainly due to unwanted coupling between adjacent segmented cells. Further analysis shows that in general 2-3 barrier ions, each confined with an optical trapping frequency of $\omega_{\rm o.t.p} \approx \omega_{\rm rad}$ are sufficient for maintaining low crosstalk levels (see the SM [46]).

A few percent crosstalk level, reflected by both $\varepsilon_{{\rm BW},b}$ and $\varepsilon_{J,b}$, marks an almost complete decoupling between

cells. Nevertheless, it is too high for high-fidelity quantum operations, and restricts performing simultaneous logical gate on distinct cells. However this crosstalk level is low enough such that it can be mitigated perturbatively in a scalable manner. Here we specifically rely on the large-scale fast (LSF) method, presented in Ref. [14].

In essence, LSF makes use of a multi-tone drive in order to generate programmable multi-qubit gates, which naively involves solving a quadratically constrained optimization problem of dimension N^2, and generates the unitary gate, $\exp\left(\sum_{n,m=1}^{N}\varphi_{n,m}\sigma_x^{(n)}\sigma_x^{(m)}\right)$, with $\sigma_x^{(n)}$ a Pauli-x operator acting on the nth qubit and $\varphi_{n,m}$ a target multi-qubit coupling matrix. The hardness of the optimization problem is mitigated in LSF with two key realizations. First, for each fixed system any non-vanishing drive solution to a special 'zero-phase' version, $\varphi_{n,m}^{(0)}=0$, of the optimization problem can be efficiently converted to a high-fidelity solution of any general problem. Second, the zero-phase solutions (ZPS) can be obtained by considering homogeneous illumination of the ion-crystal, resulting in a dimension N quadratic problem.

The operational approach of LSF is naturally adopted to our architecture, making the design of multi-qubit entanglement, simultaneously in all cells, fast and scalable. Specifically, we use LSF in order to generate ZPSs for an effective 'typical' cell of the bulk of the ion-crystal (see the SM [46]). Up to small deviations that are corrected below, this ZPS is adequate to all of the ion-crystal's cells. Using LSF, different multi-qubit gates are designed for each cell by converting the same ZPS. This classical computation can be performed fast and in parallel. After performing these steps we obtain a specific drive spectrum, for all computational and auxiliary qubits in the ion-crystal, that generates the required entanglement per-cell at once, $\exp\left(\sum_{s=1}^{S}\sum_{n,m=1}^{C}\varphi_{n,m}^{(s)}\sigma_x^{(n,s)}\sigma_x^{(m,s)}\right)$, with $\sigma_x^{(n,s)}$ a Pauli-x operator acting on the nth qubit in cell s and $\varphi_{n,m}^{(s)}$ the desired multi-qubit target of cell s.

As discussed above, the unwanted coupling between cells incurs a $\sim 2.5\%$ crosstalk error, which is dominated by nearest-neighbor cells. Here this brings about a typical coupling of $\sim 0.025\varphi_{n,m}^{(s)}$ between ions in distinct cells. Therefore we make use of an additional mitigation layer on top of LSF. Crucially, the nearest-neighbor structure of the crosstalk enables our mitigation technique to scale favorably, in terms of classical computation resources, and does not impose constraints on the ion-crystal size.

Specifically, we perform an iterative optimization by linearizing the quadratic constraints around the current solution, with the initial solution given by LSF as discussed above. The resulting linear equations provide conditions that resolve crosstalk as well as inaccuracies of the LSF solution that originate from the assumption of a typical cell. We do so locally, i.e. the linear conditions are formed for only two adjacent cells at a time, generating $C\left(C-1\right)$ linear constraints that improve the LSF results and $3C^2$ linear constraints that correspond to crosstalk terms. The iterative optimization is stopped when a target infidelity is reached. Crucially since the linear equations are local, relating only four adjacent cells at a time, they involve only $\mathcal{O}\left(C^2\right)$ linear constraints, allowing parallel optimization of the next four adjacent cells [46].

An additional condition for a high-fidelity process is decoupling of the qubits from the modes of motion at the end of the entanglement operation. This is typically satisfied by forming constraints for each of the N modes of motion independently. Here however such an approach will be a hurdle to scalability since it will be infeasible to satisfy a large N number of constraints. Instead, we make use of only $C+B_{A,B}$ linear constraints of the typical cell, and supplement these with additional robustness properties that make the decoupling insensitive to the mode frequency inaccuracies, described in Ref. [66], such that each constraint enforces the decoupling of an entire band at once.

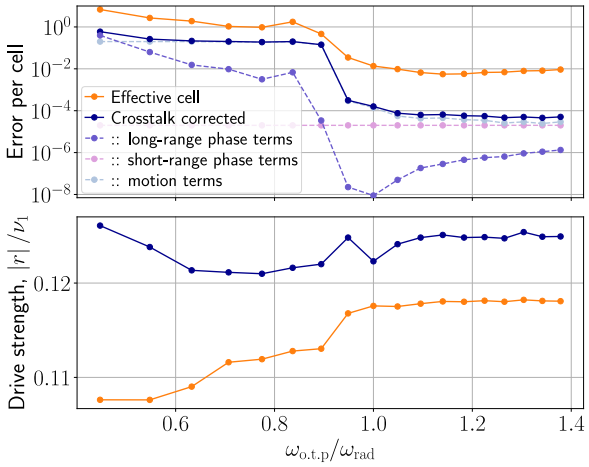

FIG. 7. Performance of the crosstalk mitigation method as a function of optical trapping potential $\omega_{\mathrm{o.t.p}}$, evaluated on the entanglement used to implement a simulation of a 3d rectangular Ising model. Top: Error per cell, using Eq. (7), as a proxy for the entanglement infidelity of the entire multi-qubit operation. For $\omega_{\mathrm{o.t.p}}\gtrsim\omega_{\mathrm{rad}}$ the crosstalk compensated solution (dark-blue) shows a low, $<10^{-4}$, infidelity. As expected, the initial LSF solution, based on the effective typical cell (orange) shows a $\sim 10^{-2}$ infidelity. The mitigation degrades in the weak optical confinement regime, due to long-range coupling between cells that is not considered in the crosstalk mitigation method. Indeed this degradation appears when considering long-range cells (dashed purple), and not seen when only considering nearest-neighbor and onsite coupling (dashed pink). Additional infidelity due to residual coupling to motional modes (dashed light-blue) exhibits a similar behavior. Bottom: The required total drive coupling, given in units of the lowest transverse mode frequency (bottom). The crosstalk compensated solution (dark-blue) only incurs a small, $\sim 10\%$, overhead on the initial LSF solution (orange).

We study the efficacy of our crosstalk mitigation method by considering a segmented ion-crystal system used for a 3d Ising model simulation, similar to that shown in Fig. 2 above, with $S = 5$, $d = 3$ and $B_A = B_B = 3$. We design the control pulses that implement the required qubit-qubit couplings, for various optical trapping frequencies. The resulting operation infidelity is evaluated, to leading order in the qubit-qubit coupling deviations and in residual ion displacements, as,

$$I = I_{\text{short}} + I_{\text{long}} + I_{\text{motion}} \tag{7}$$

such that I_{short} approximates the infidelity due an erroneous qubit-qubit coupling within each cell and crosstalk to nearest-neighbor cells, I_{long} is the infidelity due to qubit-qubit coupling between cells that are not nearest-neighbors and I_{motion} approximates the infidelity due to residual coupling between the qubits and the phonon modes of motion.

Figure 7(top) presents the infidelity, I, of the initial LSF solution, based on the typical cell (orange) and the crosstalk corrected solution (dark-blue). It exhibits an apparent cross-over between two regimes at $\omega_{\text{o.t.p}} = \omega_{\text{rad}}$, at which point the transverse mode band structure is manifested. At low optical confinement the performance of the uncorrected, typical-cell solution (orange) is low, such that our leading-order estimation breaks-down. At strong optical confinement this solution generates an infidelity of $\sim 10^{-2}$, as expected from our analysis above. However the crosstalk-corrected solution (dark-blue) successfully generates solutions that have an infidelity that is better (lower) than 10^{-4} for the entire multi-qubit operation, throughout the strong optical confinement regime.

We account for the different contributions to the crosstalk-corrected solution, given by Eq. (7). We note that I_{short} (dashed pink), has a negligible contribution, regardless of optical confinement, while I_{long} (dashed purple) converges to low values only at the strong confinement regime. This behavior is expected as our optimization actively corrects for on-site and nearest-neighbor terms, and ignores other terms. This implies that strong optical confinement successfully decouples next nearest-neighbor (and further) cells, removing the need to take the entire ion-crystal into account, and enabling scalability. Similarly, due to a well-formed band structure, the motional infidelity, I_{motion} (dashed light-blue), becomes small at strong optical confinement, and in general dominates the overall infidelity.

Figure 7(bottom) shows the total drive coupling, i.e. Rabi frequency, required to drive the initial LSF solution (orange) and the crosstalk corrected solution (dark-blue), given in terms of the frequency of the lowest radial mode, ν_1, as a characteristic scale. The compensated solution incurs a small overhead of $\sim 10\%$ on the initial solution.

We remark that our architecture and crosstalk compensation method can also be implemented by global driving of entire cells using similar techniques, such as in Refs. [12, 14].

VII. MID-CIRCUIT MEASUREMENTS

The ability to perform mid-circuit projective measurements, and apply coherent feedback based on the measured results, is at the heart of QEC, as well as additional central quantum computational tools [67–69]. In trapped-ions based systems, projective state detection is typically performed by state-dependent florescence. This poses a technical challenge, as the scattered photons usually heat-up the ion-crystal due to photon recoil. Furthermore the photon may be resonant with neighboring ions and scattered by them, resulting in decoherence of the quantum state of the entire system. Thus, so far, mid-circuit measurements have been implemented in trapped ions either in small ion-crystals, which are well separated from other parts of the quantum register, by 'shelving' all computational qubits to non-resonant atomic states, or by using two different atomic species spectraly separating logical and incoherent operations [70–73].

In our optically segmented ion-crystal scheme, optically confined ions are well-suited for mid-circuit measurements, as their motion is separated to independent bands (top part of the spectra in Figs. 4 and 5), thus photon scattering heating remains local and does not heat the other crystal modes. Furthermore, the optical fields generating the trapping also substantially light-shift the atomic transition lines of the ions, specifically the photon emission lines, such that photon scattering is largely suppressed. Thus no physical shuttling of the ions into dedicated measurement regions is required, nor the use of multiple ion-species.

We describe the protocol used to measure the qubit state of some target ions, without incurring decoherence on computational qubits, or heating of bulk modes. After the measurement is completed, we cool and re-initialize the measured ions. Figure 8 (top) illustrates these general steps involved in performing mid-circuit measurements. For simplicity we consider the required operations on three types of ions in the ion-crystal, i.e. computational qubit ions, 'C' (green), barrier ions to be measured, 'B' (light-green) and optically confined barrier ions, 'A' (purple). Crucially, our measurement method can be performed in parallel throughout the entire ion-crystal on all required ions. In our architecture ions may be optically confined specifically for the purpose of mid-circuit measurements, without having an essential role in segmentation of the ion-crystal, as showcased in the application of a QEC surface code, above.

For concreteness we consider a specific realization, in trapped $^{40}Ca^{+}$ ions. Furthermore we consider a local control over a single wavelength, at $\sim$ 400 nm, which couples the two qubit states defined in the $4S_{1/2}$ ground state manifold via Raman transitions mediated by the short lived $4P$ manifolds. This local control, acting independently on all ions, is primarily used for generating single qubit rotations and multi-qubit programmable gates, however here it is utilized as a means to 'localize' global

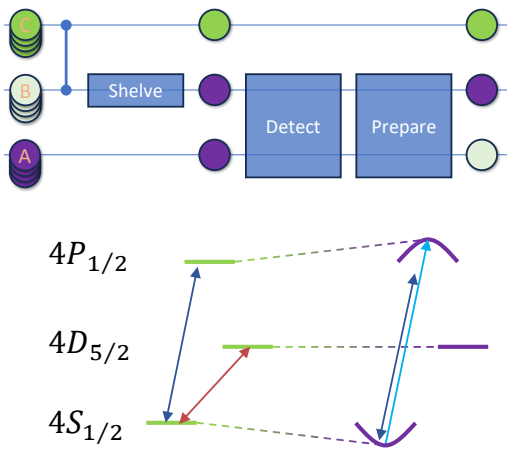

FIG. 8. Top: schematic of mid-circuit measurement protocol, showing three types of involved ions, computational qubit ions, C (green), barrier ion to be measured, B (light-green) and optically confined barrier ions, A (purple). Operations are ordered from left to right. Data is encoded on ion C (vertical line), and one of the qubit states of the ion is 'shelved' to a non-fluorescing state using local control. Next an intermediate optical segmentation configuration is used, confining both ions A and B, and separating their motion from the computational qubits. The state of the barrier ions is measured ('Detect') and then reset ('Prepare'). Lastly the optical segmentation configuration is switched. Bottom: Relevant atomic levels of $^{40}Ca^{+}$ ions, showing $4S_{1/2}$ the ground state manifold, the metastable $4D_{5/2}$ manifold and the short-lived $4P_{1/2}$ manifold. The $S \leftrightarrow P$ transition varies between the no-optical confinement (left) and optically confined (right) cases, allowing to separate the two cases spectrally (see main text). The main optical field used in the protocol are shown, namely at 729 nm (red), coupling the $S \leftrightarrow D$ levels, at 400 nm (dark-blue), generating Raman transition between qubit states as well as additional local light-shifts, and at 397 nm (light-blue) coupling the $S \leftrightarrow P$ levels.

control fields using light-shifts, detailed below. While additional local controls, that can be used in our scheme, will act to simplify the resulting mid-circuit measurement protocol, we show that a single local control remarkably suffices to facilitate all requirements.

The main atomic levels used for standard qubit operation are presented in Fig. 8 (bottom) in the case of no optical confinement (left) and with optical confinement (right). The ground state manifold is coupled to the narrow meta-stable $4D_{5/2}$ manifold via a 729 nm field (red arrow). In the case of no optical confinement, this transition can be localized by light-shifting the $4S_{1/2}$ manifold of a target ion by using the locally controlled 400 nm field (dark-blue arrow). For these purposes a small, e.g. few MHz light-shift suffices. On the other hand, optical confinement strongly light-shifts the $4S_{1/2} \leftrightarrow 4P_{1/2}$ level (right), making the 729 nm coupling off resonant. In principle, this strong shift can be taken into account, however since the $S \leftrightarrow D$ transition is narrow it imposes stringent requirements on the intensity stabilization of the optical confinement. Here we simply do not make use of the $S \leftrightarrow D$ transition for optically confined ions relaxing the requirements for intensity stabilization.

However, Raman transitions within the qubits subspace, mediated by the 400 nm field, are negligibly affected by optical confinement, and exclusively in terms of their Rabi frequency.

An additional field resonant with the $S \leftrightarrow P$ transition at 397 nm is used (light-blue). Its frequency does require adjustment to the light-shift due to optical confinement, however the P level is broad, thus the required stability of the optically confining fields is reasonable. The combination of local 400 nm and 397 nm fields, together with standard repump fields (not shown), adjusted as well for light-shifts, accommodates for all the necessary steps, i.e., state detection, various cooling techniques and state preparation.

The mid-circuit protocol shown in Fig. 8 is carried out by first encoding some information on ion B via the entanglement operations detailed above (vertical line connecting ions C and B), e.g. parity information of a plaquette shown in Fig. 3. Then, one of the qubit states of ion B is 'shelved' to the D manifold via a combination of 400 nm light-shift and 729 nm coupling, making this operation local on the ion.

Next, the segmentation configuration is changed to an intermediate setting where all barrier ions are illuminated. The purpose of optically confining ion B is to prepare it for being measured, by separating its motion from the computational qubit's motion and to light-shift its $S \leftrightarrow P$ transition. However the confinement of ion A cannot be relaxed since ion B might fully populate the D level, in which case it is not optically confined. State detection is performed using the light-shifted 397 nm field, followed by qubit reset and preparation using a combination of the 397 nm and 400 nm fields.

During the detection and preparation steps all optically confined ions scatter 397 nm photons, such that all of them are required to be cooled down in the 'prepare' step, which can be done in parallel. The scattered photons are substantially detuned, by approximately 2 GHz, from the absorption lines of the computational qubit ions, having a linewidth of few tens of MHz, thus negligibly influencing their state. Nevertheless the state of neighboring computational qubits, located few micrometers apart, may be further protected by shelving both of their qubit states to the D level (at the shelving step). Alternatively they may simply remain unutilized.

Lastly the segmentation configuration can now be changed, exchanging the roles of ions 'A' and 'B'. The cooled 'A' ions are returned to the bulk of the cells and cool-down the bulk modes via sympathetic cooling.

VIII. SUMMARY

Here we propose a scalable architecture for quantum computing; it is based on a large register of trapped-ion

qubits together with dynamically operated optical potentials. Our proposed architecture circumvents the two most prominent challenges in working with ever-larger ion-crystals – prohibitively high heating rates and spectral crowding of the ions' motional modes. It does so by effectively segmenting an arbitrarily large trapped ion-crystal into several independent segments of a manageable size. Despite the local structure that results, connectivity across the full trapped ion-crystal is enabled by rapidly reconfiguring the optical potentials. The optical potentials further enable mid-circuit measurements of the confined ions, followed by classical feedback.

The utility of this architecture is emphasized when combined with a method for programmable multi-qubit entangling gates, such as that proposed in Ref. [14]. We have used this method to numerically study the application of independent multi-qubit unitaries on each cell in parallel and in a scalable manner. Moreover we have extended this method to enable arbitrarily good compensation of crosstalk errors that arise between adjacent segments.

Our architecture requires modest hardware resources and makes use off well-established experimental techniques; it is thus an ideal platform for quantum simulation, quantum computation, as well as ultimately for fault tolerant quantum computing.

ACKNOWLEDGMENTS

This work was supported by the Israel Science Foundation Quantum Science and Technology (Grants 2074/19, 1376/19 and 3457/21).

[1] J. P. Gaebler, T. R. Tan, Y. Lin, Y. Wan, R. Bowler, A. C. Keith, S. Glancy, K. Coakley, E. Knill, D. Leibfried, and D. J. Wineland. High-fidelity universal gate set for $^{9}Be^{+}$ ion qubits. *Phys. Rev. Lett.*, 117:060505, 2016.

[2] C. J. Ballance, T. P. Harty, N. M. Linke, M. A. Sepiol, and D. M. Lucas. High-fidelity quantum logic gates using trapped-ion hyperfine qubits. *Phys. Rev. Lett.*, 117:060504, 2016.

[3] Pengfei Wang, Chun-Yang Luan, Mu Qiao, Mark Um, Junhua Zhang, Ye Wang, Xiao Yuan, Mile Gu, Jingning Zhang, and Kihwan Kim. Single ion qubit with estimated coherence time exceeding one hour. *Nature Communications*, 12(1):233, 2021.

[4] Craig R. Clark, Holly N. Tinkey, Brian C. Sawyer, Adam M. Meier, Karl A. Burkhardt, Christopher M. Seck, Christopher M. Shappert, Nicholas D. Guise, Curtis E. Volin, Spencer D. Fallek, Harley T. Hayden, Wade G. Rellergert, and Kenton R. Brown. High-fidelity bell-state preparation with $^{40}ca^{+}$ optical qubits. *Phys. Rev. Lett.*, 127:130505, 2021.

[5] R. Srinivas, S. C. Burd, H. M. Knaack, R. T. Sutherland, A. Kwiatkowski, S. Glancy, E. Knill, D. J. Wineland, D. Leibfried, A. C. Wilson, D. T. C. Allcock, and D. H. Slichter. High-fidelity laser-free universal control of trapped ion qubits. *Nature*, 597(7875):209–213, 2021.

[6] G. Pagano, P. W. Hess, H. B. Kaplan, W. L. Tan, P. Richerme, P. Becker, A. Kyprianidis, J. Zhang, E. Birckelbaw, M. R. Hernandez, Y. Wu, and C. Monroe. Cryogenic trapped-ion system for large scale quantum simulation. *Quantum Science and Technology*, 4(1), 2019.

[7] I. Pogorelov, T. Feldker, Ch. D. Marciniak, L. Postler, G. Jacob, O. Krieglsteiner, V. Podlesnic, M. Meth, V. Negnevitsky, M. Stadler, B. Höfer, C. Wächter, K. Lakhmanskiy, R. Blatt, P. Schindler, and T. Monz. Compact ion-trap quantum computing demonstrator. *PRX Quantum*, 2:020343, 2021.

[8] R. Yao, W. Q. Lian, Y. K. Wu, G. X. Wang, B. W. Li, Q. X. Mei, B. X. Qi, L. Yao, Z. C. Zhou, L. He, and L. M. Duan. Experimental realization of a multiqubit quantum memory in a 218-ion chain. *Physical Review A*, 106(6):1–6, 2022.

[9] Florian Kranzl, Manoj K. Joshi, Christine Maier, Tiff Brydges, Johannes Franke, Rainer Blatt, and Christian F. Roos. Controlling long ion strings for quantum simulation and precision measurements. *Phys. Rev. A*, 105:052426, 2022.

[10] Q. A. Turchette, Kielpinski, B. E. King, D. Leibfried, D. M. Meekhof, C. J. Myatt, M. A. Rowe, C. A. Sackett, C. S. Wood, W. M. Itano, C. Monroe, and D. J. Wineland. Heating of trapped ions from the quantum ground state. *Phys. Rev. A*, 61:063418, 2000.

[11] M. Brownnutt, M. Kumph, P. Rabl, and R. Blatt. Ion-trap measurements of electric-field noise near surfaces. *Rev. Mod. Phys.*, 87:1419–1482, 2015.

[12] Yotam Shapira, Ravid Shaniv, Tom Manovitz, Nitzan Akerman, Lee Peleg, Lior Gazit, Roee Ozeri, and Ady Stern. Theory of robust multiqubit nonadiabatic gates for trapped ions. *Phys. Rev. A*, 101:032330, 2020.

[13] Yotam Shapira, Jovan Markov, Nitzan Akerman, Ady Stern, and Roee Ozeri. Programmable quantum simulations on a trapped-ions quantum computer with a global drive, 2023.

[14] Yotam Shapira, Lee Peleg, David Schwerdt, Jonathan Nemirovsky, Nitzan Akerman, Ady Stern, Amit Ben Kish, and Roee Ozeri. Fast design and scaling of multi-qubit gates in large-scale trapped-ion quantum computers, 2023.

[15] D. Kielpinski, C. Monroe, and D. J. Wineland. Architecture for a large-scale ion-trap quantum computer. *Nature*, 417(6890):709–711, 2002.

[16] S. A. Moses, C. H. Baldwin, M. S. Allman, R. Ancona, L. Ascarrunz, C. Barnes, J. Bartolotta, B. Bjork, P. Blanchard, M. Bohn, J. G. Bohnet, N. C. Brown, N. Q. Burdick, W. C. Burton, S. L. Campbell, J. P. Campora III au2, C. Carron, J. Chambers, J. W. Chan, Y. H. Chen, A. Chernoguzov, E. Chertkov, J. Colina, J. P. Curtis, R. Daniel, M. DeCross, D. Deen, C. Delaney, J. M. Dreiling, C. T. Ertsgaard, J. Esposito, B. Estey, M. Fabrikant, C. Figgatt, C. Foltz, M. Foss-Feig, D. Francois, J. P. Gaebler, T. M. Gatterman, C. N. Gilbreth, J. Giles, E. Glynn, A. Hall, A. M. Hankin, A. Hansen, D. Hayes, B. Higashi, I. M. Hoffman,

B. Horning, J. J. Hout, R. Jacobs, J. Johansen, L. Jones, J. Karcz, T. Klein, P. Lauria, P. Lee, D. Liefer, C. Lytle, S. T. Lu, D. Lucchetti, A. Malm, M. Matheny, B. Mathewson, K. Mayer, D. B. Miller, M. Mills, B. Neyenhuis, L. Nugent, S. Olson, J. Parks, G. N. Price, Z. Price, M. Pugh, A. Ransford, A. P. Reed, C. Roman, M. Rowe, C. Ryan-Anderson, S. Sanders, J. Sedlacek, P. Shevchuk, P. Siegfried, T. Skripka, B. Spaun, R. T. Sprenkle, R. P. Stutz, M. Swallows, R. I. Tobey, A. Tran, T. Tran, E. Vogt, C. Volin, J. Walker, A. M. Zolot, and J. M. Pino. A race track trapped-ion quantum processor, 2023.

[17] D. L. Moehring, P. Maunz, S. Olmschenk, K. C. Younge, D. N. Matsukevich, L.-M. Duan, and C. Monroe. Entanglement of single-atom quantum bits at a distance. *Nature*, 449(7158):68–71, 2007.

[18] D. P. Nadlinger, P. Drmota, B. C. Nichol, G. Araneda, D. Main, R. Srinivas, D. M. Lucas, C. J. Ballance, K. Ivanov, E. Y.-Z. Tan, P. Sekatski, R. L. Urbanke, R. Renner, N. Sangouard, and J.-D. Bancal. Experimental quantum key distribution certified by bell's theorem. *Nature*, 607(7920):682–686, 2022.

[19] V. Krutyanskiy, M. Galli, V. Krcmarsky, S. Baier, D. A. Fioretto, Y. Pu, A. Mazloom, P. Sekatski, M. Canteri, M. Teller, J. Schupp, J. Bate, M. Meraner, N. Sangouard, B. P. Lanyon, and T. E. Northup. Entanglement of trapped-ion qubits separated by 230 meters. *Phys. Rev. Lett.*, 130:050803, 2023.

[20] Tobias Olsacher, Lukas Postler, Philipp Schindler, Thomas Monz, Peter Zoller, and Lukas M. Sieberer. Scalable and Parallel Tweezer Gates for Quantum Computing with Long Ion Strings. *PRX Quantum*, 1(2):1, 2020.

[21] Yu Ching Shen and Guin Dar Lin. Scalable quantum computing stabilised by optical tweezers on an ion crystal. *New Journal of Physics*, 22(5):53032, 2020.

[22] J. D. Arias Espinoza, M. Mazzanti, K. Fouka, R. X. Schüssler, Z. Wu, P. Corboz, R. Gerritsma, and A. Safavi-Naini. Engineering spin-spin interactions with optical tweezers in trapped ions. *Physical Review A*, 104(1):1–8, 2021.

[23] M. Mazzanti, R. X. Schüssler, J. D. Arias Espinoza, Z. Wu, R. Gerritsma, and A. Safavi-Naini. Trapped Ion Quantum Computing Using Optical Tweezers and Electric Fields. *Physical Review Letters*, 127(26):1–5, 2021.

[24] Yi Hong Teoh, Manas Sajjan, Zewen Sun, Fereshteh Rajabi, and Rajibul Islam. Manipulating phonons of a trapped-ion system using optical tweezers. *Physical Review A*, 104(2):1–13, 2021.

[25] M. Mazzanti, R. Gerritsma, R. J. C. Spreeuw, and A. Safavi-Naini. Trapped Ion Quantum Computing using Optical Tweezers and the Magnus Effect. 2023.

[26] Roee Ozeri. The trapped-ion qubit tool box. *Contemporary Physics*, 52(6):531–550, 2011.

[27] Colin D. Bruzewicz, John Chiaverini, Robert McConnell, and Jeremy M. Sage. Trapped-ion quantum computing: Progress and challenges. *Applied Physics Reviews*, 6(2):021314, 2019.

[28] A. Ashkin. Acceleration and trapping of particles by radiation pressure. *Phys. Rev. Lett.*, 24:156–159, 1970.

[29] Steven Chu, L. Hollberg, J. E. Bjorkholm, Alex Cable, and A. Ashkin. Three-dimensional viscous confinement and cooling of atoms by resonance radiation pressure. *Phys. Rev. Lett.*, 55:48–51, 1985.

[30] John Preskill. Quantum Computing in the NISQ era and beyond. *Quantum*, 2:79, 2018.

[31] Richard P. Feynman. Simulating physics with computers. *International Journal of Theoretical Physics*, 21(6):467–488, 1982.

[32] C. Neill, T. McCourt, X. Mi, Z. Jiang, M. Y. Niu, W. Mruczkiewicz, I. Aleiner, F. Arute, K. Arya, J. Atalaya, R. Babbush, J. C. Bardin, R. Barends, A. Bengtsson, A. Bourassa, M. roughton, B. B. Buckley, D. A. Buell, B. Burkett, N. Bushnell, J. Campero, Z. Chen, B. Chiaro, R. Collins, W. Courtney, S. Demura, A. R. Derk, A. Dunsworth, D. Eppens, C. Erickson, E. Farhi, A. G. Fowler, B. Foxen, C. Gidney, M. Giustina, J. A. Gross, M. P. Harrigan, S. D. Harrington, J. Hilton, A. Ho, S. Hong, T. Huang, W. J. Huggins, S. V. Isakov, M. Jacob-Mitos, E. Jeffrey, C. Jones, D. Kafri, K. Kechedzhi, J. Kelly, S. Kim, P. V. Klimov, A. N. Korotkov, F. Kostritsa, D. Landhuis, P. Laptev, E. Lucero, O. Martin, J. R. McClean, M. McEwen, A. Megrant, K. C. Miao, M. Mohseni, J. Mutus, O. Naaman, M. Neeley, M. Newman, T. E. O'Brien, A. Opremcak, E. Ostby, B. Pató, A. Petukhov, C. Quintana, N. Redd, N. C. Rubin, D. Sank, K. J. Satzinger, V. Shvarts, D. Strain, M. Szalay, M. D. Trevithick, B. Villalonga, T. C. White, Z. Yao, P. Yeh, A. Zalcman, H. Neven, S. Boixo, L. B. Ioffe, P. Roushan, Y. Chen, and V. Smelyanskiy. Accurately computing the electronic properties of a quantum ring. *Nature*, 594(7864):508–512, 2021.

[33] G. Semeghini, H. Levine, A. Keesling, S. Ebadi, T. T. Wang, D. Bluvstein, R. Verresen, H. Pichler, M. Kalinowski, R. Samajdar, A. Omran, S. Sachdev, A. Vishwanath, M. Greiner, V. Vuletić, and M. D. Lukin. Probing topological spin liquids on a programmable quantum simulator. *Science*, 374(6572):1242–1247, 2021.

[34] Youngseok Kim, Andrew Eddins, Sajant Anand, Ken Xuan Wei, Ewout van den Berg, Sami Rosenblatt, Hasan Nayfeh, Yantao Wu, Michael Zaletel, Kristan Temme, and Abhinav Kandala. Evidence for the utility of quantum computing before fault tolerance. *Nature*, 618(7965):500–505, 2023.

[35] Christian Kokail, Christine Maier, Rick van Bijnen, Tiff Brydges, Manoj K Joshi, Petar Jurcevic, Christine A Muschik, Pietro Silvi, Rainer Blatt, Christian F Roos, et al. Self-verifying variational quantum simulation of lattice models. *Nature*, 569(7756):355–360, 2019.

[36] W. L. Tan, P. Becker, F. Liu, G. Pagano, K. S. Collins, A. De, L. Feng, H. B. Kaplan, A. Kyprianidis, R. Lundgren, W. Morong, S. Whitsitt, A. V. Gorshkov, and C. Monroe. Domain-wall confinement and dynamics in a quantum simulator. *Nature Physics*, 17(6):742–747, 2021.

[37] Antonis Kyprianidis, Francisco Machado, William Morong, Patrick Becker, Kate S Collins, Dominic V Else, Lei Feng, Paul W Hess, Chetan Nayak, Guido Pagano, et al. Observation of a prethermal discrete time crystal. *Science*, 372(6547):1192–1196, 2021.

[38] M. K. Joshi, F. Kranzl, A. Schuckert, I. Lovas, C. Maier, R. Blatt, M. Knap, and C. F. Roos. Observing emergent hydrodynamics in a long-range quantum magnet. *Science*, 376(6594):720–724, 2022.

[39] Mu Qiao, Zhengyang Cai, Ye Wang, Botao Du, Naijun Jin, Wentao Chen, Pengfei Wang, Chunyang Luan, Erfu Gao, Ximo Sun, Haonan Tian, Jingning Zhang, and Kihwan Kim. Observing frustrated quantum magnetism in two-dimensional ion crystals. *arXiv preprint arXiv:2204.07283*, 2022.

[40] Yotam Shapira, Tom Manovitz, Nitzan Akerman, Ady

Stern, and Roee Ozeri. Quantum simulations of interacting systems with broken time-reversal symmetry. *Phys. Rev. X*, 13:021021, 2023.

[41] Mohsin Iqbal, Nathanan Tantivasadakarn, Ruben Verresen, Sara L. Campbell, Joan M. Dreiling, Caroline Figgatt, John P. Gaebler, Jacob Johansen, Michael Mills, Steven A. Moses, Juan M. Pino, Anthony Ransford, Mary Rowe, Peter Siegfried, Russell P. Stutz, Michael Foss-Feig, Ashvin Vishwanath, and Henrik Dreyer. Creation of non-abelian topological order and anyons on a trapped-ion processor, 2023.

[42] Qiming Wu, Yue Shi, and Jiehang Zhang. Qubits on programmable geometries with a trapped-ion quantum processor, 2023.

[43] D. Porras and J. I. Cirac. Effective quantum spin systems with trapped ions. *Phys. Rev. Lett.*, 92:207901, 2004.

[44] Iñigo Arrazola, Julen S. Pedernales, Lucas Lamata, and Enrique Solano. Digital-analog quantum simulation of spin models in trapped ions. *Scientific Reports*, 6(1), 2016.

[45] Tom Manovitz, Yotam Shapira, Nitzan Akerman, Ady Stern, and Roee Ozeri. Quantum simulations with complex geometries and synthetic gauge fields in a trapped ion chain. *PRX Quantum*, 1:020303, 2020.

[46] See supplemental material for additional derivation details.

[47] Emanuel Knill, Raymond Laflamme, and Wojciech H. Zurek. Resilient quantum computation. *Science*, 279(5349):342–345, 1998.

[48] A.Yu. Kitaev. Fault-tolerant quantum computation by anyons. *Annals of Physics*, 303(1):2–30, 2003.

[49] Dorit Aharonov and Michael Ben-Or. Fault-tolerant quantum computation with constant error rate. *SIAM Journal on Computing*, 38(4):1207–1282, 2008.

[50] Dominic Horsman, Austin G Fowler, Simon Devitt, and Rodney Van Meter. Surface code quantum computing by lattice surgery. *New Journal of Physics*, 14(12):123011, 2012.

[51] Alexander Erhard, Hendrik Poulsen Nautrup, Michael Meth, Lukas Postler, Roman Stricker, Martin Stadler, Vlad Negnevitsky, Martin Ringbauer, Philipp Schindler, Hans J. Briegel, Rainer Blatt, Nicolai Friis, and Thomas Monz. Entangling logical qubits with lattice surgery. *Nature*, 589(7841):220–224, 2021.

[52] Sergey Bravyi, Andrew W. Cross, Jay M. Gambetta, Dmitri Maslov, Patrick Rall, and Theodore J. Yoder. High-threshold and low-overhead fault-tolerant quantum memory, 2023.

[53] Rudolf Grimm, Matthias Weidemüller, and Yurii B. Ovchinnikov. Optical dipole traps for neutral atoms. volume 42 of *Advances In Atomic, Molecular, and Optical Physics*, pages 95–170. Academic Press, 2000.

[54] Michael Johanning. Isospaced linear ion strings. *Applied Physics B*, 122(4):71, 2016.

[55] S. K. Lamoreaux. Thermalization of trapped ions: A quantum perturbation approach. *Phys. Rev. A*, 56:4970–4975, 1997.

[56] D.J. Wineland, C. Monroe, W.M. Itano, D. Leibfried, B.E. King, and D.M. Meekhof. Experimental issues in coherent quantum-state manipulation of trapped atomic ions. *Journal of Research of the National Institute of Standards and Technology*, 103(3):259, 1998.

[57] B. E. King, C. S. Wood, C. J. Myatt, Q. A. Turchette, D. Leibfried, W. M. Itano, C. Monroe, and D. J. Wineland. Cooling the collective motion of trapped ions to initialize a quantum register. *Phys. Rev. Lett.*, 81:1525–1528, 1998.

[58] Daniel F. V. James. Theory of heating of the quantum ground state of trapped ions. *Phys. Rev. Lett.*, 81:317–320, 1998.

[59] D Kalincev, L S Dreissen, A P Kulosa, C-H Yeh, H A Fürst, and T E Mehlstäubler. Motional heating of spatially extended ion crystals. *Quantum Science and Technology*, 6(3):034003, 2021.

[60] Anders Sørensen and Klaus Mølmer. Quantum computation with ions in thermal motion. *Phys. Rev. Lett.*, 82:1971–1974, 1999.

[61] Anders Sørensen and Klaus Mølmer. Entanglement and quantum computation with ions in thermal motion. *Phys. Rev. A*, 62:022311, 2000.

[62] Nikolas P. Breuckmann and Jens Niklas Eberhardt. Quantum low-density parity-check codes. *PRX Quantum*, 2:040101, 2021.

[63] David Schwerdt, Yotam Shapira, Tom Manovitz, and Roee Ozeri. Comparing two-qubit and multiqubit gates within the toric code. *Phys. Rev. A*, 105:022612, 2022.

[64] Sergey Bravyi, Dmitri Maslov, and Yunseong Nam. Constant-cost implementations of clifford operations and multiply-controlled gates using global interactions. *Phys. Rev. Lett.*, 129:230501, 2022.

[65] Pascal Baßler, Matthias Zipper, Christopher Cedzich, Markus Heinrich, Patrick H. Huber, Michael Johanning, and Martin Kliesch. Synthesis of and compilation with time-optimal multi-qubit gates. *Quantum*, 7:984, 2023.

[66] Yotam Shapira, Ravid Shaniv, Tom Manovitz, Nitzan Akerman, and Roee Ozeri. Robust entanglement gates for trapped-ion qubits. *Phys. Rev. Lett.*, 121:180502, 2018.

[67] Robert B. Griffiths and Chi-Sheng Niu. Semiclassical fourier transform for quantum computation. *Phys. Rev. Lett.*, 76:3228–3231, 1996.

[68] Arthur G. Rattew, Yue Sun, Pierre Minssen, and Marco Pistoia. The Efficient Preparation of Normal Distributions in Quantum Registers. *Quantum*, 5:609, 2021.

[69] Tsung-Cheng Lu, Leonardo A. Lessa, Isaac H. Kim, and Timothy H. Hsieh. Measurement as a shortcut to long-range entangled quantum matter. *PRX Quantum*, 3:040337, 2022.

[70] Philipp Schindler, Julio T. Barreiro, Thomas Monz, Volckmar Nebendahl, Daniel Nigg, Michael Chwalla, Markus Hennrich, and Rainer Blatt. Experimental repetitive quantum error correction. *Science*, 332(6033):1059–1061, 2011.

[71] V. Negnevitsky, M. Marinelli, K. K. Mehta, H.-Y. Lo, C. Flühmann, and J. P. Home. Repeated multi-qubit readout and feedback with a mixed-species trapped-ion register. *Nature*, 563(7732):527–531, 2018.

[72] C. Ryan-Anderson, J. G. Bohnet, K. Lee, D. Gresh, A. Hankin, J. P. Gaebler, D. Francois, A. Chernoguzov, D. Lucchetti, N. C. Brown, T. M. Gatterman, S. K. Halit, K. Gilmore, J. A. Gerber, B. Neyenhuis, D. Hayes, and R. P. Stutz. Realization of real-time fault-tolerant quantum error correction. *Phys. Rev. X*, 11:041058, 2021.

[73] Tom Manovitz, Yotam Shapira, Lior Gazit, Nitzan Akerman, and Roee Ozeri. Trapped-ion quantum computer with robust entangling gates and quantum coherent feedback. *PRX Quantum*, 3:010347, 2022.

[74] Farhang Haddadfarshi and Florian Mintert. High fidelity

quantum gates of trapped ions in the presence of motional heating. *New Journal of Physics*, 18(12):123007, 2016.
[75] A. E. Webb, S. C. Webster, S. Collingbourne, D. Bretaud, A. M. Lawrence, S. Weidt, F. Mintert, and W. K. Hensinger. Resilient entangling gates for trapped ions. *Phys. Rev. Lett.*, 121:180501, 2018.

IX. SUPPLEMENTAL MATERIAL

A. Mode structure calculations

Mode structure, i.e. motional mode frequencies and mode participation matrices are generated by diagonalizing a classical Hamiltonian. Specifically we consider an isospaced RF trapped ion-crystal, of ions with mass m and charge e. Optical trapping potentials are taken into account by incorporating an additional on-site potential term for illuminated ions. In all of our examples in the main text and below we have considered equally-spaced trapped $^{40}Ca^{+}$ ions, with an inter-ion distance of 5 μm and a 400 nm optical field that generates the additional confinement and segmentation.

We assume the ion-crystal forms a stable linear chain, such that axial and transverse modes can be considered independently. Thus, following Ref. [54], for axial modes we write the secular matrix,

$$V_{n,m}^{\text{axial}} = \begin{cases} -2\frac{eE_{\text{n.n}}}{d|n-m|^3} & n \neq m \\ 4\zeta(3)\frac{eE_{\text{n.n}}}{d} + \frac{1}{2}m\omega_{\text{o.t.p}}^2 b_n & n = m \end{cases}, \tag{8}$$

with $b_n = 1$ ($b_n = 0$) if ion n is (not) illuminated by an optical potential, d the distance between ions, $\zeta(3) \approx 1.202$ is Apéry's constant, $E_{\text{n.n}} = \frac{e}{4\pi\epsilon_0 d^2}$ is the electric field strength created by nearest-neighbor ions and ϵ_0 is the vacuum permittivity. The eigenvalues of V^{axial} are $\frac{1}{2}m\omega_{\text{a}}^2$, with ω_{a} the axial motional mode frequencies. The eigenvectors are normal-modes of motion associated with the corresponding frequency, designated in the main text as the mode-matrix A.

Similarly, transverse (radial) modes are calculated by diagonalizing the matrix,

$$V_{n,m}^{\text{radial}} = \begin{cases} \frac{eE_{\text{n.n}}}{d|n-m|^3} & n \neq m \\ -2\zeta(3)\frac{eE_{\text{n.n}}}{d} - \frac{1}{2}m\left(\omega_{\text{rad}}^2 + \omega_{\text{o.t.p}}^2 b_n\right) & n = m \end{cases}, \tag{9}$$

with $\frac{1}{2}m\omega_{\text{rad}}^2$ the radial trapping potential generated by the RF trap, which in the analysis presented here is fixed at $\omega_{\text{rad}} = 3$ MHz. Figures 4 and 5 of the main text are generated by computing and diagonalizing the matrices in Eqs. (8) and (9).

The resulting transverse mode-matrix R, is the orthogonal matrix that diagonalizes the secular matrix in Eq. (9) and is used in the main text to estimate crosstalk between segments. This is realized by considering the mode-dependent qubit-qubit coupling (Eq. (5) of the main text),

$$J_b^{(c,s),(c',s')} = \sum_{m=1}^{S} R_{(b,m)}^{(c,s)} R_{(b,m)}^{(c',s')}, \tag{10}$$

Figure 9 highlights the resulting structure of the J_b's for several bands, with the horizontal and vertical axes representing ion indices within the ion-crystal (excluding B_A barrier ions). Specifically the 'zig-zag', $b = 0$, band (left) the COM, $b = 34$, band (right) and an intermediate, $b = 17$, band (middle). Couplings are shown in a symlog scale (colors represent a logarithmic scale in both the positive and negative directions from the origin, with an interval between $\pm 10^{-6}$ that is linearly scaled). All of the presented coupling maps show considerable inter-cell coupling and negligible crosstalk, i.e. coupling between ions in different segments, with nearest-neighbor segments constituting the most relevant correction. Furthermore long-wavelength, i.e. high b, modes generate more crosstalk, as is also shown in Fig. 5 of the main text.

B. Excitation rate calculations

In order to evaluate the excitation rate of a given axial mode of motion we recall Eq. (3) of the main text, i.e. in presence of some electric field noise, $\delta E(t, r)$, the excitation rate for a given motional mode is [11],

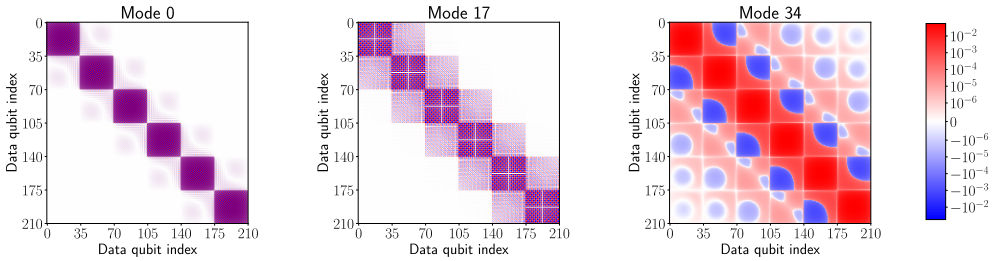

FIG. 9. Band-dependent qubit-qubit coupling, J_b. Horizontal and vertical axes are indices of qubits within the entire ion-crystal (excluding B_A barrier ions). Couplings are shown in a symlog scale (colors represent a logarithmic scale in both the positive and negative directions from the origin, with an interval between $\pm 10^{-6}$ that is linearly scaled). The optical segmentation generates a block-diagonal structure, that signifies strong coupling within each cell and negligible coupling between qubits in different cells. Couplings due to three bands are shown, the 'zig-zag' $b = 0$ band (left), the COM $b = 34$ band (right) and an intermediate band (center). Clearly crosstalk, seen as coupling outside of the diagonal blocks, is more relevant for high b, long wavelength modes.

$$\Gamma^{(k)} = \frac{e^2}{4m\hbar\omega_k} S_E^{(k)}(\omega_k), \tag{11}$$

with ω_k the frequency of mode k and $S_E^{(k)}(\omega_k)$ the spectral density of the electric field noise, given by,

$$S_E^{(k)}(\omega_k) = 2\sum_{i,j}\int d\tau \langle \delta E_k^i(\tau)\, \delta E_k^j(0)\rangle e^{-i\omega_k\tau}. \tag{12}$$

Here $\delta E_k^i(\tau)$ is the projection of δE on the kth mode of motion at the position of ion i, i.e. $\delta E_k^i(t) = \delta E(t, r_i) A_k^{(i)}$ and r_i is the position of the ith ion.

We assume that the leading order contribution to δE is spatially uniform and neglect all other contributions. Furthermore, motivated by theoretical and experimental results we assume that $S_E^{(k)} \propto \omega_k^{-\alpha}$, with α here set to 1.

This considerably simplifies $\Gamma^{(k)}$ and enables us to obtain the total axial excitation rate shown in Eq. (4) of the main text, up to a proportionality factor,

$$\Gamma \propto \sum_k \Gamma^{(k)} \propto \sum_k \frac{e^2}{4m\hbar\omega_k^2} \sum_{i,j} A_k^{(i)} A_k^{(j)}. \tag{13}$$

Crucially, the effect of optical segmentation comes about spectrally in the formation of bands, such that the summation on k in Eq. (13) can be decomposed as,

$$\Gamma \approx \sum_{b=1}^{B+C} \frac{e^2}{4m\hbar\omega_b} \sum_{s=1}^{S} \sum_{i,j} A_{b,s}^{(i)} A_{b,s}^{(j)} + \mathcal{O}\left(\frac{\mathrm{BW}_b}{\Delta\omega_b}\right), \tag{14}$$

with $A_{b,s}^{(i)}$ a re-arrangement of A according to the band structure and the error term due to the bandwidth of the bands, BW_b and the gap between bands, $\Delta\omega_b$, which is assumed to be small. From a mode-structure point of view, the optical segmentation comes about as an independent motion between adjacent cells (shown in Fig. 9), thus the sum on s restricts i and j to the same cell, leading to a linear scaling with S.

C. Crosstalk mitigation method

We provide further details on our approach to mitigating crosstalk between cells in the optically-segmented ion-crystal. In order to do so we recall some basic facts about the operation of the LSF method, which is discussed in detail in Ref. [14]. We assume the ions are driven by local fields that, in the spectral domain, all have the same M tone pairs, but can vary in the amplitude of each pair. Thus the drive is described by a set of vectors $\mathbf{r}_n$ such that

$(\mathbf{r}_n)_m$ is the amplitude of the mth tone pair that drives the nth ion. This choice of degrees of freedom allows to generate a bi-partite multi-qubit entanglement operation of the form,

$$U = \exp\left(\sum_{n,m=1}^{N} \varphi_{n,m}\sigma_x^{(n)}\sigma_x^{(m)}\right), \tag{15}$$

with $\varphi_{n,m}$ a completely controlled 'target' operation and $\sigma_x^{(n)}$ a Pauli-x operator acting on the nth ion.

Indeed, generating U can be mapped to finding solutions (of the $\mathbf{r}_n$'s) to the quadratic constraints,

$$\mathbf{r}_n^T A_{n,m}\mathbf{r}_m = \varphi_{n,m} \quad 1 \le n < m \le N, \tag{16}$$

with $A_{n,m}$ a set of real-valued $M \times M$ symmetric matrices that quantify the coupling between ions n and m due to the drive's spectral components. Specifically these coupling matrices are given by,

$$A_{n,m} = \sum_{j=1}^{N} R_j^{(n)} R_j^{(m)} A_j, \tag{17}$$

with A_j a set of real-valued $M \times M$ symmetric matrices that quantify the coupling between the drive's spectral components and mode j [12]. Typically we will be interested in solutions to small norm $\mathbf{r}_n$'s that satisfy Eq. (16), which constitutes a NP-hard optimization problem.

In LSF we make use of a given non-trivial solution, $\mathbf{r}_n = \mathbf{z}$ for all $n = 1, .., N$, that generates the target $\varphi_{n,m}^{(0)} = 0$ for all n and m, coined the zero-phase solution (ZPS). Then, solutions to other 'full' arbitrary targets can be efficiently converted from $\boldsymbol{z}$. Crucially the ZPS does not depend on the ion index, n, and thus can be found directly by considering the A_j's (instead of the $A_{n,m}$'s), reducing the number of quadratic constraints that are required to be satisfied.

We utilize these concepts and apply them to the optically-segmented ion-crystal. Generally we consider a 'typical' effective cell as an independent ion-crystal and find a ZPS for it. We then convert the ZPS to solutions to full targets, which reflect the required operations on the different cells, i.e. $U_{s,n}^{(A,B)}$ in Fig. 1 of the main text. By simply setting these solutions as the drive of the optically segmented ion-crystal we obtain entanglement gates of the form of Eq. (15), up to $\sim 10^{-2}$ infidelity, which arises mainly due to crosstalk between adjacent cells, but also due to using a typical cell system (e.g. cells at the edge of the ion-crystal are slightly different than in the bulk).

To construct a typical cell system of the ion-crystal, we consider a fictitious system that has $C + B_B$ equally spaced ions with corresponding transverse motional modes. The mode frequencies are constructed from the average frequency of each band in the motional spectrum band structure of the segmented ion-crystal. The mode participation matrix is constructed by similarly averaging the participation of each ion in each mode, partitioned to cells. The segmented ion-crystal has S modes per band (and not a single mode), which needs to be taken in to account by the typical cell system. Indeed we do so by writing our drive degrees of freedom in a way that is resilient to small inaccuracies in the motional frequency [66, 74, 75].

This construction, along with other fixed system parameters such as the entanglement gate time, ion type etc., is sufficient in order to construct A_j's and $A_{n,m}$'s of a typical cell, and to generate ZPS of it. We remark that we do not make use of tones that lie within bands since these will generate a differential coupling between the different modes within a band, and are not well approximated by the typical cell system.

We use LSF to convert the typical cell ZPS to different target cell solutions for the various cells, and obtain a set of amplitudes, $\boldsymbol{r}_{s,c}^{(0)}$ corresponding to the drive of qubit c in cell s. The qubit-qubit coupling between ions c (c') in cell s (s'), 'inherited' from the typical LSF solution, can be evaluated as, $\varphi_{(s,c),(s',c')}^{(i)} = \left(\mathbf{r}_{s,c}^{(i)}\right)^T A_{(s,c),(s',c')}\boldsymbol{r}_{s',c'}^{(i)}$, with designating the LSF solution as $i = 0$.

The resulting couplings are compared to the intended target, $\Delta\varphi_{(s,c),(s',c')}^{(i)} = \varphi_{(s,c),(s',c')}^{(i)} - \varphi_{(s,c),(s',c')}^{t}$, with the 't' inscription referring to the required ideal target dictated by the intended unitary operator, such that, $\varphi_{(s,c),(s'\neq s,c')}^{t} = 0$. Nearest-neighbor cell crosstalk errors are given by, $\Delta\varphi_{(s,c),(s\pm1,c')}^{(i)}$, and target inaccuracies are given by, $\Delta\varphi_{(s,c),(s,c')}^{(i)}$.

Since the total infidelity is small, crosstalk and target inaccuracies can be mitigated by linearizing the quadratic constraints in Eq. (16) and iteratively improving the resulting fidelity. Specifically we consider an iteration of the form $\boldsymbol{r}_{s,c}^{(i+1)} = \boldsymbol{r}_{s,c}^{(i)} + \boldsymbol{\delta}_{s,c}^{(i+1)}$, starting from $i = 0$. We construct a set of linear equations for the correction $\boldsymbol{\delta}^{(i+1)}$. In order to make this technique scalable we want to avoid considering all N ions in the ion-crystal in the same set of linear equations. This is made possible by that fact that crosstalk is dominated by coupling to nearest-neighbor cells (see Fig. 5 in the main text and Fig. 9).

Specifically we focus on two adjacent 'target' cells, s and $s+1$, and derive linear equations for them. These are,

$$\left(\boldsymbol{\delta}_{s,c}^{(i+1)}\right)^T A_{(s,c),(s,c')}\boldsymbol{r}_{s,c'}^{(i)} + \left(\boldsymbol{\delta}_{s,c'}^{(i+1)}\right)^T A_{(s,c),(s,c')}\boldsymbol{r}_{s,c}^{(i)} = \Delta\varphi_{(s,c),(s,c')}^{(i)} \tag{18}$$

$$\left(\boldsymbol{\delta}_{s+1,c}^{(i+1)}\right)^T A_{(s+1,c),(s+1,c')}\boldsymbol{r}_{s+1,c'}^{(i)} + \left(\boldsymbol{\delta}_{s+1,c'}^{(i+1)}\right)^T A_{(s+1,c),(s+1,c')}\boldsymbol{r}_{s+1,c}^{(i)} = \Delta\varphi_{(s+1,c),(s+1,c')}^{(i)} \tag{19}$$

$$\left(\boldsymbol{\delta}_{s,c}^{(i+1)}\right)^T A_{(s,c),(s+1,c')}\boldsymbol{r}_{s+1,c'}^{(i)} + \left(\boldsymbol{\delta}_{s+1,c'}^{(i+1)}\right)^T A_{(s,c),(s+1,c')}\boldsymbol{r}_{s,c}^{(i)} = \Delta\varphi_{(s,c),(s+1,c')}^{(i)} \tag{20}$$

$$\left(\boldsymbol{\delta}_{s,c}^{(i+1)}\right)^T A_{(s,c),(s-1,c')}\boldsymbol{r}_{s-1,c'}^{(i)} = \Delta\varphi_{(s,c),(s-1,c')}^{(i)} \tag{21}$$

$$\left(\boldsymbol{\delta}_{s+1,c}^{(i+1)}\right)^T A_{(s+1,c),(s+2,c')}\boldsymbol{r}_{s+2,c'}^{(i)} = \Delta\varphi_{(s+1,c),(s+2,c')}^{(i)}. \tag{22}$$

with $c, c' = 1, .., C$. The first (second) row accounts for inaccuracies of the target implemented on cell s ($s+1$), the third row accounts for crosstalk between cells s and $s+1$, and the forth (fifth) row accounts for crosstalk between cell s ($s+1$) and cell $s-1$ ($s+2$). The choice to correct the drive of two adjacent cells simultaneously is since this construction allows crosstalk between cells s and $s+1$ to be mitigated simultaneously by both $\boldsymbol{\delta}_{s,c}$ and $\boldsymbol{\delta}_{s+1,c'}$, which has been found to be more efficient than the correction of the crosstalk with control over a single qubit drive, e.g. the terms in the fourth and fifth rows.

Crucially all of these terms result in $C\,(C-1)+3C^2$ linear constraints, and are independent of the total number of segments. Moreover iterative optimizations can be performed by considering independent blocks of 4 adjacent cells, that can be efficiently parallelized and interlaced. We remark that an additional linear constraint can be added in order to minimize the amplitude of the $\boldsymbol{r}_n$'s [14].

We perform f optimization iterations, until convergence of the solution, or until meeting a fidelity criteria. We use the resulting solutions and benchmark the expected fidelity of the corresponding entanglement operations. The resulting infidelity is evaluated, in leading order, as,

$$I = I_{\text{short}} + I_{\text{long}} + I_{\text{motion}} \tag{23}$$

$$I_{\text{short}} = 2\sum_{s=1}^{S}\sum_{c,c'=1}^{C+B_B}\left(\left|\Delta\varphi_{(s,c),(s,c')}^{(f)}\right|^2 + \left|\Delta\varphi_{(s,c),(s+1,c')}^{(f)}\right|^2 + \left|\Delta\varphi_{(s,c),(s-1,c')}^{(f)}\right|^2\right) \tag{24}$$

$$I_{\text{long}} = 2\sum_{s=1}^{S}\sum_{s'\neq s,s\pm1}^{S}\sum_{c,c'=1}^{C+B_B}\left|\Delta\varphi_{(s,c),(s',c')}^{(f)}\right|^2 \tag{25}$$

$$I_{\text{motion}} = \sum_{j=1}^{N}\sum_{n=1}^{N}\left|\alpha_j^{(n)}\right|, \tag{26}$$

with I_{short} representing the residual unwanted coupling between qubits that is accounted for by our mitigation iterations, I_{long} representing the residual unwanted coupling between qubits that is not accounted for by our mitigation, and I_{motion} accounting for unwanted residual displacement of the $j = 1, ..., N$ motional modes. Here $\alpha_j^{(n)}$ is the displacement of mode j due to ion n and is thus linearly related to the $\boldsymbol{r}_n$s and can be easily evaluated [12, 14]. While we are not directly controlling and minimizing the latter term in our optimization iterations, the resilience to motional frequency errors of the typical cell, discussed above, ensures that it remains small.

D. Crosstalk and power analysis

We analyze the dependence of the crosstalk, in its mode-structure dependent formulation, $\varepsilon_{\text{J},b}$ in Eq. (6) of the main text, on the choice of the number of barrier ions per cell, B_A, and on the optical confining power used per barrier ion, $\omega_{\text{o.t.p}}/\omega_{\text{rad}}$. The comparison to the radial RF trapping frequency, ω_{rad}, is a natural scale for analyzing crosstalk in entanglement operations that utilize transverse modes of motion.

Figure 10 (left) shows the mean crosstalk averaged over all bulk-bands, $\langle\varepsilon_{\text{J},b}\rangle_b$ (color), for a segmented ion-crystal made of $S = 4$ segments, each containing $C = 32$ computational qubits and B (horizontal axis) barrier ions, such that each barrier ion is illuminated by an optical confining potential with a trapping frequency $\omega_{\text{o.t.p}}$ (vertical axis). Clearly, as the optical trapping frequency decreases the mean crosstalk increases, and passes the perturbative limit, set here to 0.1 (white dashed). We also present constant lines of the expression, $P = B\omega_{\text{o.t.p}}^2/\omega_{\text{rad}}^2$, as it is proportional to the total required optical power per-cell (colored lines, see value of P in the legend).

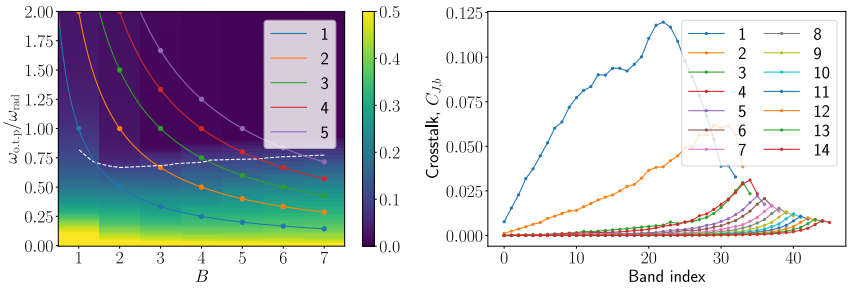

FIG. 10. Crosstalk dependence on $\omega_{\mathrm{o.t.p}}$ and B. Left: Mean crosstalk (colored regions) for varying number of barrier ions (horizontal axis) and varying optical confinement, $\omega_{\mathrm{o.t.p}}$, per barrier ions, given in units of the RF radial trapping, ω_{rad} (vertical axis). We observe that a perturbative crosstalk, set for values below 0.1 (area above white dashed line), is generated by setting $\omega_{\mathrm{o.t.p}} \geq 0.75\omega_{\mathrm{rad}}$, almost regardless of B. Nevertheless increasing B is helpful in reducing the crosstalk. The total optical power per cell is proportional to $P = B\omega^2_{\mathrm{o.t.p}}/\omega^2_{\mathrm{rad}}$ (colored lines, with the values of P in the legend). Right: Estimation of band-dependent crosstalk, $\varepsilon_{J,b}$, based on mode structure analysis in an ion-crystal with cell size of $C = 32$ qubits and $S = 4$ segments, and a varying number of barrier ions, $B_A = B_B$ (color). In general the addition of barrier ions decreases the overall crosstalk in the system. Limiting cases are found for $B_A = 1, 2$ in which some of the collective modes do not involve the barrier ions, resulting in a non-typical crosstalk structure. Clearly for $B_A \geq 3$ this behavior is suppressed. The mean crosstalk of the curves with of $1 \leq B \leq 5$ at $\omega_{\mathrm{o.t.p}} = \omega_{\mathrm{rad}}$ are correspondingly shown in the left.

Figure 10 (right) shows $\varepsilon_{J,b}$ for $C = 32$, $S = 4$ and various values of B_A, between 1 and 14 (color), such that for all B_A barrier ions $\omega_{\mathrm{o.t.p}}/\omega_{\mathrm{rad}} = 1$. The curves show expected crosstalk due to $b = 1, .., C + B_B$ bands, with $B_B = B_A$, similarly to the inset of Fig. 5. The high-index cell bands are typically the main contributors to the crosstalk as they correspond to long-wavelength excitations of the cells, analogues to low-order oscillating multipoles, thus having a stronger coupling to adjacent cells. Clearly, a larger barrier reduces the overall crosstalk. Nevertheless, the curves do not show a monotonic behavior, which is especially obvious with $B_A = 1$ (blue) and $B_A = 2$ (orange), which exhibit resonant-like features. These resonances are likely due to the modes of motion in which the barrier-ions only weakly participate and therefore cannot isolate the motion of ions within a single cell. For $B_A \geq 3$ this effect is generally suppressed, leading to only a residual distance-dependent Coulomb interaction between the cells. Furthermore, since our crosstalk mitigation technique relies on linearization, we have to work in the perturbative crosstalk regime, which is already shown to apply at $B_A \geq 2$, motivating our choices in the main text.